INTELLIGENT POWER ELECTRONICS (IPE) FOR HIGH POWER QUALITY OF ELECTRICITY IN URBAN AREAS WITH HIGH FRACTION OF RENEWABLES

(IQ-GRID)

Prepared by,

Rohan Deshmukh, Arturo Martinez Lopez, Miad Ahmadi, Robin van der Sande, Gautam Rituraj, Hani Vahedi, Aditya Shekhar, Olindo Isabella, and Pavol Bauer

Electrical Sustainable Energy Department

Faculty of Electrical Engineering, Mathematics and Computer Science,
Delft University of Technology, Delft, The Nederlands.

CONTENTS

1

INTRODUCTION

1.1. BACKGROUND

It is stated by Alliander and Energy research Centre of the Netherlands (ECN) in the FLEXNET project report [1], "Despite a limited total number of overloaded assets the regional distribution grids face great challenges in the form of large numbers of new connections for EV charging points, local congestion due to local concentrations of EV, PV and/or HP, a large increase of connections for medium size solar and wind farms, and the phase out of gas in the built environment that creates the need and natural moment to adapt the electricity grid... Geographically, most overloads are expected to arise in city centres, because of relatively old networks. The fact that the adoption of PV, EV and HP is lower in the city centres is offset by the density of the urban population, resulting in a larger increase of power load in urban areas than in non-urban areas..."

In a few decades, the Dutch government aims to achieve low-carbon energy management and create new, sustainable economic growth opportunities. This aim requires transitioning to large-scale utilization of renewable energy sources (RES), such as solar and wind energies. These sources will provide a potentially unlimited amount of clean electricity in urban areas for households and factories and new areas of electricity applications such as transportation, heating, and industrial processes. The consequence of this development is that the existing electrical energy system has to undergo significant changes since it cannot accommodate these developments. Technologies generating electricity from solar and wind energy must be developed together with components and devices such as cables for direct current (DC), inverters, and charge controllers that couple the electricity from these RES into the existing power grid that is based on alternating current (AC) [2, 3].

The energy flow through the electricity network is often referred to as power. It is of utmost importance that the electrical loads operate under power conditions that do not cause malfunction or damage to these devices. The proper power conditions are expressed as power quality. The power quality involves magnitude, frequency, harmonics, and resonance of the grid voltage. RES and new loads significantly influence the power quality and need more attention than ever. The reasons include:

- The intermittent nature of RES. It is well known that RES relies heavily on weather conditions, primarily solar and wind energy, which is well-established. The significant fluctuations in power output from RES can result in voltage flicker or frequency variation of the grid [1].
- Heavy and instant power demand of the fast charger. To shorten the charging time of EVs and make them more competitive than ICE cars, a fast charger is being developed, which usually operates at 200-300 kW in a few minutes. Considering the capacity of the distribution grid in the neighborhood, such a load is relatively large and can also lead to a variation in the grid voltage frequency [2].
- Many power harmonics introduced by the power electronics converters of the RES and electric loads, e.g., e-houses, e-transportation, etc. More and more power converters are connected to the grid, where their switching behavior brings EMC-EMI issues, and their power filters can resonance with the grid [3, 4].

In order to maintain the high power quality in the grid based on electricity from RES combined with storage, it is required to map the electrical requirements of new loads, such as fast charging of batteries of electric vehicles, batteries for residential storage, or processes for converting power to molecules for long-term energy storage. To increase the flexibility of the grid, many power electronic converters have to become autonomous assets that utilize real-time analytics, which can perform on-board execution models and ensure energy-supplying quality for urban areas.

1.2. OBJECTIVES

The proposed IQ-GRID project report aims at maintaining high power quality in grids with a large fraction of electricity from RES and unconventional loads. This is achieved by designing and developing intelligent power electronic (IPE) devices to integrate the DC transmission network into the existing AC network, ensuring high power quality of energy supply for urban areas. The primary goal of this project is to secure high electric power quality in urban networks with significant utilization of energy from RES. This goal will be achieved by designing and developing IPE devices that will perform autonomous regulation or demand-response control in order to cope with the intermittent nature of RES and the increase of, among others, energy storage, electric-vehicle chargers, e-public transportation, and e-housing in the network. The specific objectives are as follows:

- Mapping electrical requirements of loads and electricity generators, such as fast charging of batteries in electric vehicles, systems for electricity generation from RES, high power electric transportation in urban areas, all-electric houses, processes for converting power to gas for energy storage
- Analysing the influence of loads and electricity generating technologies on the power quality of the urban energy network,
- Developing design rules for power electronic systems that meet electrical requirements of the above-mentioned different applications,

- Developing methods for monitoring power quality in a specific part of the grid,
- Design and fabricate intelligent power electronic converters with a focus on grid-friendly actions,
- Test the fabricated power electronic converter and validate their performance for maintaining and controlling high power quality of the urban grid.

1.3. EXPECTED RESULTS

An autonomous improvement of the power quality in urban networks is expected by designing and developing intelligent power-electronic systems, such as the ones used in RE conversion systems, electric vehicle fast chargers, e-transport, and e-houses. In the course of the project, the following results will be demonstrated (TRL 4 will be reached):

- Identification and modeling of the typical urban area energy network and their inner components: electricity sources, loads, cabling, transformers, etc. This will be used for mapping and understanding the urban network performance on power quality,
- Development of flexible and intelligent power electronic hardware and control algorithms which can incorporate both grid-friendly functionalities and their normal work purpose,
- Methods allowing power electronic components to safely monitor the power quality in a specific part of the grid, e.g., at the places where the parts are connected,
- Design, fabrication, and testing of power electronic systems for validation of the study.

1.4. OUTLINE OF THE REPORT

This report comprises six chapters, where the first and last chapters are introduction and conclusion, respectively. Rest four central chapters contains the work related to the expected results discussed in Section 1.3.

To achieve the results mentioned above, the formulated four main work packages (WPs) in this project have been translated into four central chapters (i.e., 2-5) in this report. Chapter 2 (WP2) deals with mapping E-loads and RES and their influence on power quality. Chapter 3 (WP3) explains the design rules for IPE components for controlling power quality in urban networks. Chapter 4 (WP4) presents IPE measurement of grid power quality and data sharing. Chapter 5 (WP5) discusses a case study and development of IPE components. Finally, the conclusions are given in Chapter 6.

REFERENCES

[1] ECN & Alliander, The demand for flexibility of the power system in the Netherlands, 2015-2050 - Report of phase 1 of the FLEXNET project, 2017.

[2] https://energietrends.info/wp-content/uploads/2016/09/EnergieTrends2016.pdf.

[3] Alexandre Lucas, Fausto Bonavitacola, Evangelos Kotsakis, Gianluca Fulli, “Grid harmonic impact of multiple electric vehicle fast charging,” Electric Power Systems Research, Vol. 127, Pages 13-21, 2015.

[4] S. Izadkhast, P. Garcia-Gonzalez, P. Frías, P. Bauer, L. Ramírez-Elizondo, “Evaluation of aggregate models of plug-in electric vehicles for primary frequency control,” International Journal of Automotive Technology and Management, vol. 18, no. 3, pp.270 – 294, 2018.

[5] L. Beloqui Larumbe, Z. Qin and P. Bauer, "Introduction to the Analysis of Harmonics and Resonances in Large Offshore Wind Power Plants," 2018 IEEE 18th International Power Electronics and Motion Control Conference (PEMC), Budapest, Hungary, 2018, pp. 393-400.

[6] N. H. Van Der Blij, L. M. Ramirez-Elizondo, M. T. J. Spaan and P. Bauer, "Stability and Decentralized Control of Plug-and-Play DC Distribution Grids," in IEEE Access, vol. 6, pp. 63726-63736, 2018.

[7] S. Bandyopadhyay, L. Ramirez-Elizondo and P. Bauer, "Stability Constrained Gain Optimization of Droop Controlled Converters in DC Nanogrids," 2018 International Power Electronics Conference (IPEC-Niigata 2018 -ECCE Asia), Niigata, Japan, 2018, pp. 1426-1434.

[8] W.-Y. Chang, “The State of Charge Estimating Methods for Battery: A Review” in Applied Mathematics, 2013.

[9] L. Lam and P. Bauer, "Practical Capacity Fading Model for Li-Ion Battery Cells in Electric Vehicles," in IEEE Transactions on Power Electronics, vol. 28, no. 12, pp. 5910-5918, Dec. 2013.

2

WP2: Mapping E-Loads and RES and Their Influence on Power Quality

2.1. Introduction

The emissions of greenhouse gases especially CO_2 have increased drastically over a few years. As a result, there has been a collective effort to reduce these emissions with the emphasis on diminishing their detrimental impacts on the climate including the increase in average global temperature. In the Netherlands, the Klimaatakkoord aims at the reduction of CO_2 emissions by 49% in 2030 and 95% in 2050 relative to the 1990 levels [1]. This is well aligned with the targets set by the European Union (EU) with regards to the climate and therefore, is within the framework of other international agreements, like the Paris Agreement [2, 3].

One does not fulfill such targets with ease and therefore, several transformations are inevitable in industries around the world. The intensive research in renewable energy systems indicates the potential of renewable electricity for the efficient and carbon-free operation of such industries. Moreover, modes of transportation such as road and rail have been able to integrate with renewable energy systems such as wind and solar[4, 5]. However, this has not been the case for water and air transportation as they rely heavily on carbon based fuels. Therefore, carbon recycling can prove to be a potential solution in reducing CO_2 emissions.

The reduction in CO_2 can be achieved in two ways: thermo-chemical conversion into carbon-based products and fuels and, CO_2 electrolysis. Power electronics-based electrolysis systems have tremendous potential if energy-dense fuels are produced with renewable electricity. Solutions up to the MW range in industries have been developed[6]. In [7], the challenges and future trends of low-temperature electrolysis have been discussed. Here, the study of various system architectures along with a review of converter topologies for high-power electrolysis has been carried out. According to their study,

a direct three-phase AC inverter is preferred for a grid-connected system, a current-doubler secondary for parallel cell connection and a multi-port converter for independent connection architecture.

This study aims to introduce the concept of adaptive modularity in power electronics converters utilized for such applications. Electrolysis requires low voltage and very high current. Figure 2.1 provides the system structure for this study. The system specifications considered for future prototype development are shown in Table 2.1. A Pho-

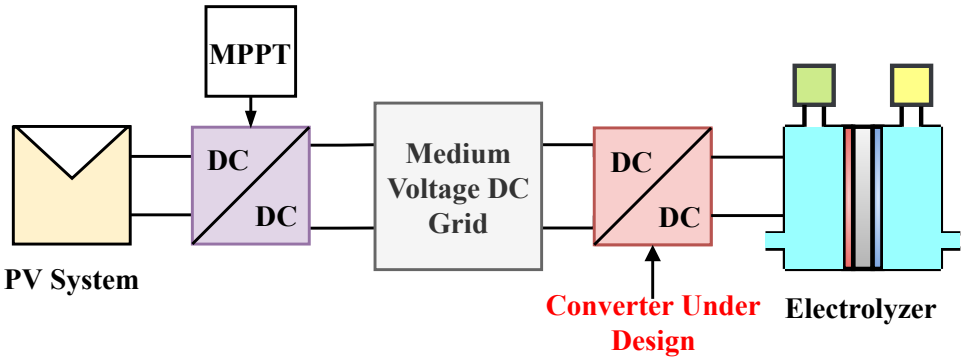

Figure 2.1: Structure of the electrolyzer system.

Table 2.1: System specifications considered for future prototype development

Parameter	Value
Input Voltage	1.4 kV
Rated Power	100 kW
Expected Stack Voltage	70 V

tovoltaic (PV) system is integrated with the medium voltage direct-current (MVDC) grid with the help of a DC-DC converter operating on the principle of Maximum Power Point Tracking (MPPT). An additional DC-DC converter acts as a power electronics interface (PEI) between the MVDC grid and the electrolyzer.

This chapter is organized as follows: Section 2.2 provides a literature review of state-of-the-art electrolyzers. Section 2.3 explains the electrical modelling process for an alkaline electrolyzer along with a sensitivity analysis with 4 degrees of freedom. Moreover, converter design challenges, trade-offs and operational challenges have been reported. Section 2.4 provides a review of the studied converter topologies in the literature. Section 2.5 explains the concept of adaptive modularity and how it can be applied to the considered configurations. Section 2.6 provides various possible system architectures reported in the literature for the electrolyzer systems. Section 2.8 provides conclusions.

2.2. STATE-OF-THE-ART ELECTROLYZERS

2.2.1. ALKALINE ELECTROLYZERS

Alkaline electrolyzer technology is the most widely used and mature technology [8–10]. In this design, the electrodes are placed as close as possible to the diaphragm to ensure that the gases produced on both sides, escape the electrodes at the rear. Caustic Potash (Potassium Hydroxide, 20 - 30 % conc.) along with water is used as an electrolyte [11]. Gas separators are installed on both sides of the diaphragm for the collection of H_2 at the cathode and O_2 gas at the anode. Water is fed on both sides of the diaphragm with the help of pumps. Figure 2.2 shows the cell design of an alkaline electrolyser. The half re-

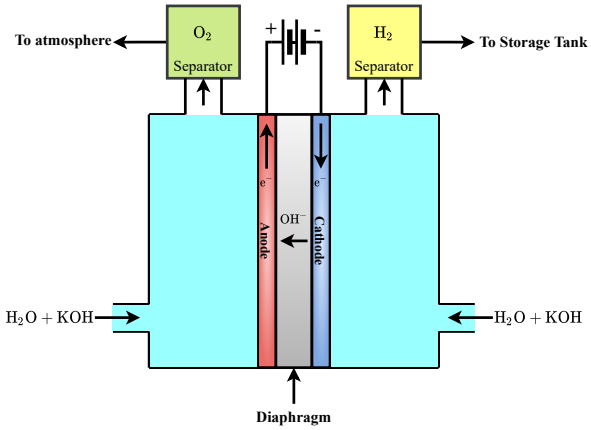

Figure 2.2: Alkaline electrolyser Structure

actions governing the process of alkaline electrolysis at cathode and anode respectively are shown below:

$$2\,H^+ + 2\,e^- \longrightarrow H_2 \qquad \text{(Cathode)} \tag{2.1}$$

$$2\,OH^- \longrightarrow \frac{1}{2}\,O_2 + H_2O + 2\,e^- \qquad \text{(Anode)} \tag{2.2}$$

The H_2 and O_2 gas obtained at the cathode and anode respectively are passed through gas separators to filter out any residual water vapour or other any impurities present for obtaining the purest yield.

2.2.2. PROTON EXCHANGE MEMBRANE

General Electric developed the first PEM electrolyzer based on the solid porous electrode concept in the 1960s [12]. This was based on the concept introduced by Thomas Grubb, where a solid sulfonated polystyrene membrane was used as an electrolyte [13, 14]. As the name suggests, the PEM electrolysis cell allows the transportation of protons from the anode to the cathode. Unlike, the hydroxyl ions moving from the cathode to anode in alkaline electrolysers, the PEM electrolyser as the name suggests allows the transportation of protons from the anode to the cathode. The polymer electrolyte membrane

(Nafion®, fumapem®) is responsible for offering high proton conductivity, low gas cross-over, compact system design and high pressure operation. Figure 2.3 shows the structure of a PEM electrolyser. The half-reactions governing the process of water electrolysis at

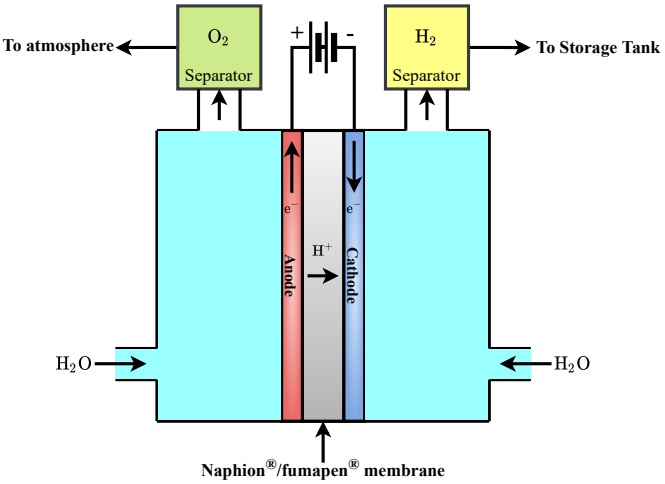

Figure 2.3: Proton Exchange Membrane Electrolyser Structure

the cathode and anode, respectively are shown below:

$$2\,H^+ + 2\,e^- \longrightarrow H_2 \qquad \text{(Cathode)} \qquad (2.3)$$

$$H_2O \longrightarrow 2\,H^+ + \frac{1}{2}\,O_2 + 2\,e^- \qquad \text{(Anode)} \qquad (2.4)$$

2.2.3. SOLID OXIDE ELECTROLYZER (SOEC)

The process of solid oxide electrolysis was reported by Dönitz and Erdle as part of the HotElly project at Dornier System GmbH in the 1980s [15]. The RELHY project [16] targeted the development of novel or improved, low-cost materials (and the related manufacturing process) for SOECs. This research indicated that the materials developed could be operated at high temperatures and could be used for the electrolysis of CO_2 to CO, and also the co-electrolysis of H_2O/CO_2 to H_2/CO (syngas).

The half reactions governing the process of water electrolysis at the cathode and anode respectively are shown below [17]:

$$2\,H_2O + 4\,e^- \longrightarrow 2\,H_2 + 2\,O_2^- \qquad \text{(Cathode)} \qquad (2.5)$$

$$2\,CO_2 + 4\,e^- \longrightarrow 2\,CO + 2\,O_2^- \qquad \text{(Cathode)} \qquad (2.6)$$

$$2\,O_2^- \longrightarrow O_2 + 4\,e^- \qquad \text{(Anode)} \qquad (2.7)$$

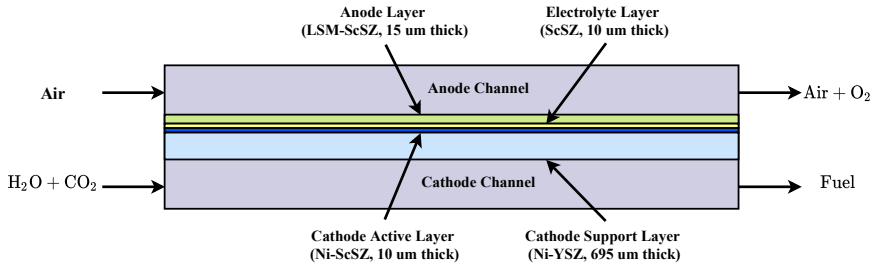

(a) Traditional structure

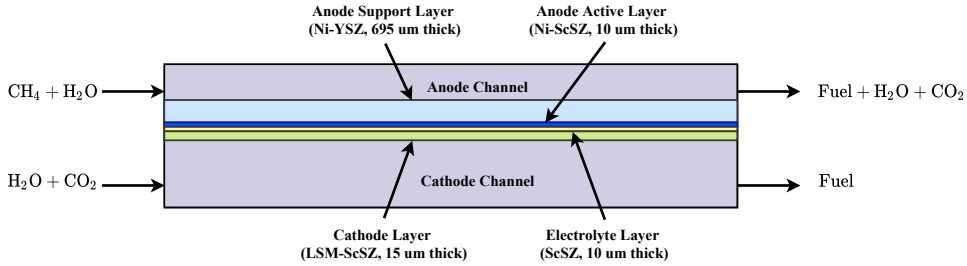

(b) CH_4 assisted structure

Figure 2.4: Solid oxide electrolyser [17]

2.3. ELECTRICAL MODELLING OF AN ALKALINE ELECTROLYZER

To get a preliminary insight a pre-defined alkaline electrolyzer system will be utilized. Several modelling approaches have been shown in literature [10, 18–20]. Despite some differences, every approach divides the cell modelling mainly into four steps. The approach followed in [19] will be applied to this study. The voltage across an electrolysis cell is developed as a result of the contributions made by the following four potentials:

2.3.1. REVERSIBLE POTENTIAL

The reversible potential of alkaline electrolysis cells exhibits a thermodynamic effect. The reversible potential is given by the Nernst Equation:

$$V_{rev} = V^0_{rev,T_k} + \frac{RT_k}{zF} \ln\left(\frac{P_{H_2}\sqrt{P_{O_2}}}{P_{H_2O}}\right) \tag{2.8}$$

In case, the electrolyte contains an alkali such as KOH. Equation 2.8 can be rewritten as follows:

$$V_{rev} = V^0_{rev,T_k} + \frac{RT_k}{zF} \ln\left(\frac{(P - P_{KOH}) \cdot \sqrt{P - P_{KOH}}}{a_{H_2O,KOH}}\right) \tag{2.9}$$

where V_{rev} is defined as the reversible cell voltage, V. V^0_{rev,T_k} is defined as the temperature dependent reversible voltage, V. R is known as the universal gas constant, $JK^{-1}mol^{-1}$. T_k is the cell temperature, K. P is the absolute pressure, bar. z is defined as the number of

moles of electrons transferred for 1 mol of product. F is the Faraday constant, C mol^{-1}. P_{KOH} is the vapour pressure of KOH, bar. $a_{H_2O,KOH}$ is known as the water activity of KOH solution. As observed in Equation 2.8, the reversible cell potential can further be divided into two types of reversible cell potentials:

- Temperature dependent cell potential at a reference standard pressure (1 bar), V^0_{rev,T_k}.
- Logarithmic dependence, accounting for the pressure dependence and non-idealities of the process due to the vapour pressures of H_2 and O_2.

The expressions for reversible voltage, vapour pressure of H_2O and KOH and, water activity of the KOH solution are given below:

$$V^0_{rev,T_k} = 1.5184 - (1.5421 \times 10^{-3} \cdot T_k) + (9.526 \times 10^{-5} \cdot T_k \cdot \ln(T_k)) + (9.84 \times 10^{-8} \cdot T_k^2) \tag{2.10}$$

$$P_{H_2O} = \exp\left(81.618 - \frac{7699.7}{T_k} - 10.9 \cdot \ln(T_k) + 9.589 \times 10^{-3} \cdot T_k\right) \tag{2.11}$$

$$P_{KOH} = \exp\left(2.302 \cdot a + b \cdot \ln(P_{H_2O})\right) \tag{2.12}$$

$$a_{H_2O,KOH} = \exp\left(-5.192 \times 10^{-2} \cdot m + 3.302 \times 10^{-3} \cdot m^2 + \frac{3.177m - 2.131m^2}{T_k}\right) \tag{2.13}$$

where,

$$a = -1.51 \times 10^{-2} m - 1.6788 \times 10^{-3} m^2 + 2.2588 \times 10^{-5} m^3 \tag{2.14}$$

$$b = 1 - 1.2062 \times 10^{-3} m + 5.6024 \times 10^{-4} m^2 - 7.8228 \times 10^{-6} m^3 \tag{2.15}$$

2.3.2. ACTIVATION POTENTIAL

Activation potential refers to the interaction of electrolyte (chemical species) and electrodes via electrical charges. Figure 2.5 shows this interaction in detail. In this figure, the electrons are received by the electrodes from the power supply, and therefore, they begin to accumulate. As a result of this concentration, potassium ions (positive polarity) get attracted towards this electrode. A condition is reached where the charge on the electrode is compensated by an equal amount of charge provided by the potassium ions. This process leads to the formation of a double-layer effect [21]. In continuous DC operation, the activation phenomena are represented in the form of a non-linear voltage[22, 23]. However, the approach followed in [19] represents this as a parallel combination of a capacitor (electrode capacitance) and voltage-controlled current source for each electrode.

The activation potential of both electrodes can be represented by the modified Tafel

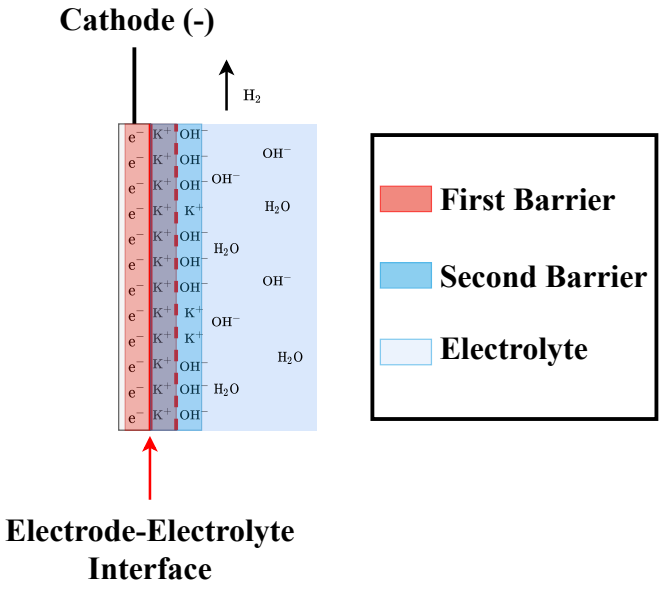

Figure 2.5: Double layer effect at cathode

Equations:

$$V_{\text{act(ano)}} = s \ln\left(\frac{i_{\text{act(ano)}}}{t} + 1\right) \tag{2.16}$$

$$V_{\text{act(cat)}} = v \ln\left(\frac{i_{\text{act(cat)}}}{w} + 1\right) \tag{2.17}$$

where s, t, v, w are temperature dependent constants. $i_{\text{act(ano)}}$ and $i_{\text{act(cat)}}$ are activation currents for anode and cathode respectively. The temperature-dependent constants are determined with the help of curve-fitting and experimental data in contrast to the traditional exchange current density parameter due to the significant variation in the numerical values used in the literature [24].

$$s = s_1 + s_2 T_c + s_3 T_c^2 \tag{2.18}$$

$$t = t_1 + t_2 T_c + t_3 T_c^2 \tag{2.19}$$

$$v = v_1 + v_2 T_c + v_3 T_c^2 \tag{2.20}$$

$$w = w_1 + w_2 T_c + w_3 T_c^2 \tag{2.21}$$

Electrode's capacitance can be obtained by electrochemical impedance spectroscopy (EIS), which is done by injecting a small-signal current perturbation at a wide range of frequencies and measuring the voltage [19].

2.3.3. OHMIC POTENTIAL

Ohmic potential refers to the internal resistance offered by the electrolyte across the electrodes. This is represented by a temperature-dependent resistance.

$$V_{\text{ohm}} = i_{\text{cell}} \cdot R_{\text{ohm}} = i_{\text{cell}} \frac{r}{A_{\text{elect}}} \tag{2.22}$$

where, r is the area-specific resistance of one of the electrolysis cells, (Ωm^2) and therefore, can be obtained from the experimental static current-voltage (I-V) characteristics at different temperatures of the electrolyzer with the help of curve-fitting techniques. i_{cell} is the cell current, A. A_{elect} is the electrode surface area, m^2. R_{ohm} is the internal resistance of the electrolyzer cell, Ω.

In order to initiate the curve fitting technique, a starting value for r is obtained with the help of the small signal current perturbation technique, where, each instantaneous voltage step is divided by the instantaneous current step in accordance with Ohm's law. This resistance value can, therefore, be calculated since this component responds instantaneously.

$$r = r_1 + r_2 T_c + \frac{r_3}{T_c} + \frac{r_4}{T_c^2} \tag{2.23}$$

2.3.4. DIFFUSION POTENTIAL

Diaphragms or membranes utilized in electrolyzers are used to ensure that the products (gases/water molecules) obtained on both sides do not diffuse into each other. However, these components are not perfect, and therefore, when the process is carried out at high currents and pressure, these products tend to diffuse into each other. This develops an over-potential that occurs due to the concentration difference between the two electrodes and initiates diffusion. For instance, water molecules diffuse from anode to cathode through the polymer membrane in the PEM electrolyzer [25, 26]. This diffusion leads to an inefficient operation. The electrolyzer which is to be modelled is an alkaline electrolyzer and hence, this contribution has not been considered.

2.3.5. CELL VOLTAGE

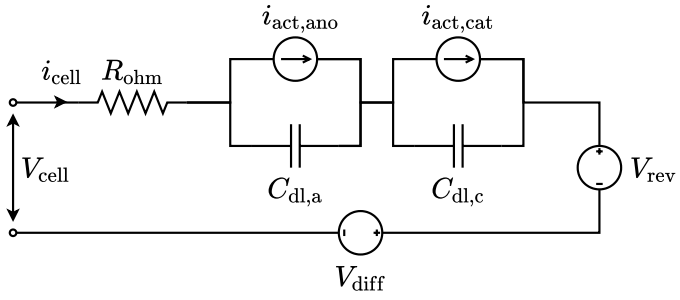

Figure 2.6: Detailed equivalent circuit of the electrolysis cell.

In case of the detailed model illustrated in Figure 2.6, the cell voltage is given by,

$$V_{\text{cell}} = V_{\text{rev}} + V_{\text{ohm}} + V_{\text{act}} + V_{\text{diff}} \tag{2.24}$$

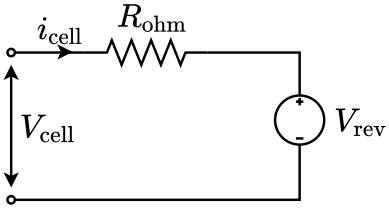

Figure 2.7: Simplified equivalent circuit of the electrolysis cell.

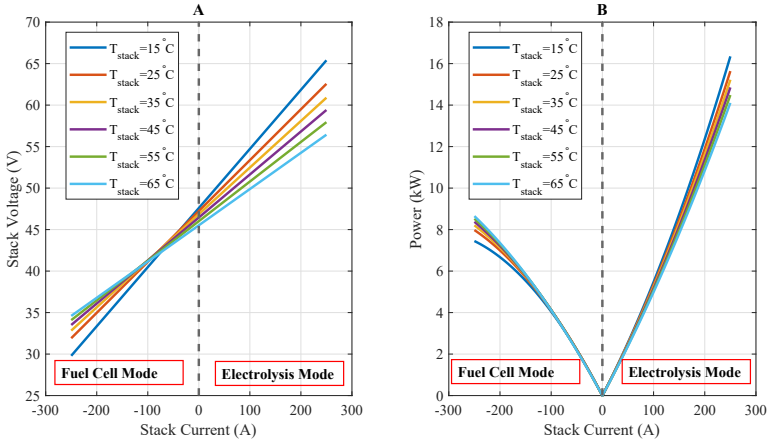

Figure 2.8: Simplified Electrical Characteristics of the Regenerative Alkaline Stack, (A): Current-Voltage Characteristics; (B): Current-Power Characteristics.

The activation and diffusion potentials have been neglected to simplify the modelling process. As a result, the resulting equivalent circuit can be redrawn as shown in Figure 2.7. The cell voltage can then be computed as follows:

$$V_{\text{cell}} = V_{\text{rev}} + V_{\text{ohm}}. \tag{2.25}$$

This approach is extended to make a regenerative stack of N_s series-connected cells.

Characteristics shown in Figure 2.8 do not give complete information about the behaviour of the regenerative stack. Therefore, it is important to study the effects of varying certain parameters of the regenerative stack on its electrical characteristics. For this study, the parameters considered are stack temperature, electrode surface area, number of series connected cells, and molar concentration of the electrolyte. Table 2.2 summarises the potential converter design challenges and trade-offs for high-power electrolysis based on the results of the sensitivity analysis of the alkaline regenerative stack.

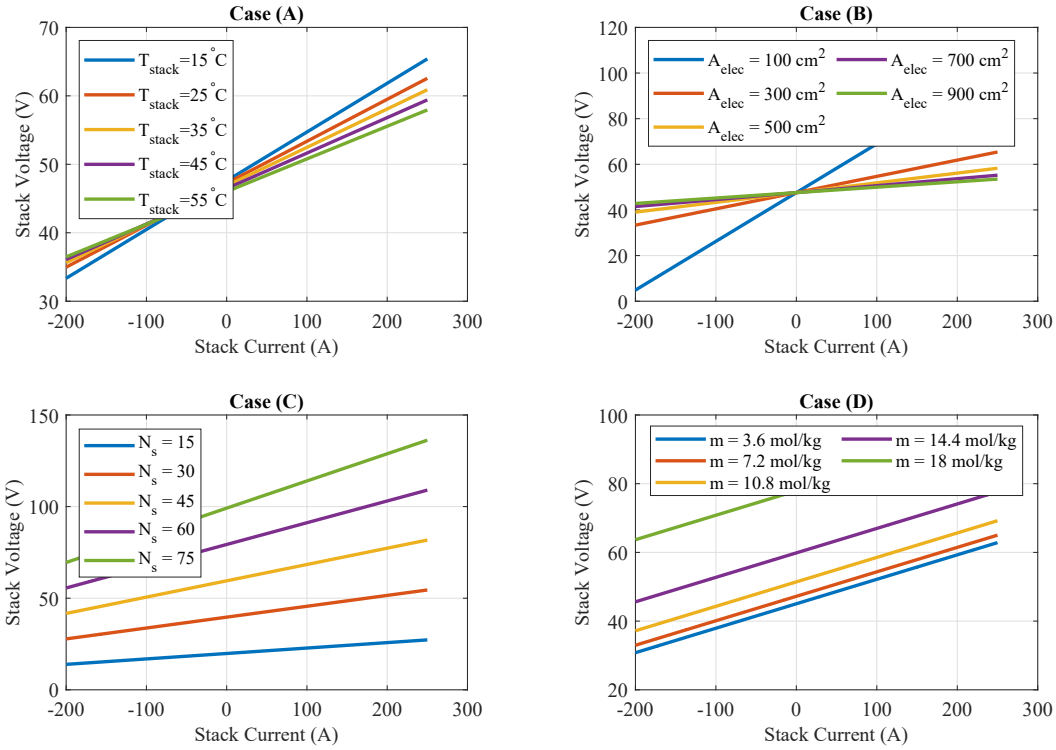

Figure 2.9: Sensitivity analysis results for the considered alkaline regenerative stack, Case (A): Impact of stack temperature; Case (B): Impact of electrode surface area; Case (C): Impact of a number of series connected cells; Case (D): Impact of molar concentration.

Table 2.2: Converter Design Challenges, Preferences and Trade-Offs for High Power Electrolysis

Parameter	**Effect on electrical characteristics**	**Preference from converter design perspective**	**Challenges/Trade-offs**
Stack temperature	Higher stack temperature increases ion mobility thereby, increasing the stack current.	Temperature of 15°C would be preferred to have a higher stack voltage for achieving a lower operating current for the given rated operating power to reduce the conduction losses in the converter	The hydrogen production rate reduces with decrease in stack temperature[27].
Electrode Surface area	Influences the stack current in accordance to Cottrell's Equation[28]. Internal resistance is inversely proportional to the surface area and directly proportional to the distance between the two electrodes in accordance to Ohm's law.	Curve corresponding to A_{elec} = 100 cm^2 would be preferred as it provides the highest possible stack voltage at a lower operating current for the same rated operating power. This implies lower losses in converter and stack as well as component derating in current magnitude.	A smaller electrode surface area strongly influences the internal resistance thereby, leading to higher losses in the electrolyzer. For A_{elec}= 100 cm^2, a boundary breach was detected where the internal resistance of the electrolyzer increased drastically. This is due to it's dependence on the distance between the electrodes as well as their surface area.
Number of series connected cells	Influences the reversible stack voltage as well as the internal resistance.	Higher number of series connected cells is preferred to achieve a higher stack voltage so that a lower operating current is achieved for the given rated operating power as this can lower converter current rating and lower losses.	Limitations are imposed on this parameter due to issues associated with equalizing fuel/gas pressure within the cells[29].
Molar concentration of electrolyte	Influences the stack voltage and therefore, the internal resistance of the electrolyzer.	An electrolyte with higher molar concentration would be preferred to achieve a higher stack voltage so that a lower operating current is achieved for the given rated operating power.	Periodic purging of electrolyte is essential in an alkaline electrolyzer. This ensures that the molar concentration is maintained. The amount of electrolyte that can be injected into the system is defined by the reservoir capacity. This is desirable only at an industrial scale. In residential applications, water can be used as a substitute for an alkaline electrolyte and a cyclic process is achieved wherein hydrogen is generated, stored and utilized to produce electricity and water. However, in the case of water, the curves shown in Case C will be at a much lower stack voltage which is not desirable from the perspective of converter design. Moreover, increasing the molar concentration increases the viscosity of an electrolyte. This may result in higher electrical losses in circulating pumps as they have to do more work for circulating this electrolyte.

2.3.6. OPERATIONAL CHALLENGES

In Figure 2.8 (B), the power rating of the stack during the fuel cell mode of operation is much smaller than the power rating during the electrolysis cell mode of operation resulting in an asymmetrical characteristic of the stack. This is because of the voltage drop across the internal resistance and current direction [30]. More importantly, the area that is bounded by these curves for a given temperature defines the operating region of the converter under design. The converter must be highly efficient over this wide operating region.

In addition to these challenges, the converter must be able to provide galvanic isolation in accordance with ISO22734:2020 standard for hydrogen generators using water electrolysis and ISO19880-1:2020 standard for gaseous hydrogen fueling stations makes it obligatory for the frames and enclosures to be grounded that become energized under first fault conditions. The transformer under design would have a large turns ratio, so leakage inductance will be dominant. The switch selection must be carried out appropriately based on the maximum thermal handling capability which indirectly defines the current handling capability as conduction losses will be dominant on the stack side.

2.4. CONVERTER TOPOLOGY

DC-DC converters can be mainly classified on the basis of the ability to provide galvanic isolation[31]. It is necessary for this study to have an isolated DC-DC converter in accordance with the standards discussed in the previous section. Therefore, a review of isolated DC-DC converters will be carried out.

In [32] a DC-DC converter topology consisting of a full-bridge converter and a rectifier was proposed. The fuel cell is connected to the full-bridge converter which is interfaced with the rectification unit via a multi-winding transformer. The leakage inductance introduced in the circuit due to the inclusion of this transformer is utilized for incorporating Zero-Voltage-Switching (ZVS) in the full bridge. The secondary side consists of multiple electro-mechanical relays that control the transformation ratio. The relay operation is stack voltage-dependent. A 3 kW prototype was developed and an efficiency of 96.5%. The transformer losses accounted for 50% of the total losses at 1 kW, and the losses in Metal Oxide Semi-Conductor Field Effect Transistors (MOSFET) accounted for 20%. However, it should be noted that the rectification unit consists of diodes, and therefore, power flow is unidirectional.

Seoul National University of Technology proposed a design for integrating fuel cells with residential loads [33]. The design had 3 stages namely, a front-end DC-DC converter, a DC-AC converter, and an auxiliary power supply operated by a bi-directional DC-DC converter. Phase-shifted ZVS was utilized for this topology to minimize switching losses, and the series connection of DC outputs allowed the reduction of the transformer turns ratio. The reported efficiency was found to be 90 %. However, MOSFETs in high voltage (HV) bridges are required to carry the full load current and therefore, they need to have higher thermal handling capability. The transformers on the primary side are branched after the full bridge and therefore, control over the branch currents is lost. As a result, this topology requires appropriate control such that power is evenly distributed among the transformers. More importantly, ZVS is no longer applicable at lighter loads and, therefore, leads to high switching losses in the MOSFETs.

Virginia Tech [34] proposed a topology that consisted of 3 full bridges on the primary side and 3-phase uncontrolled rectifiers on the secondary side. A 3-phase transformer has been utilized for this design. Reported efficiency was 96 %. This topology does not suffer from the issue of operating at lighter loads in comparison to the topology discussed in [33]. Nevertheless, it has a similar problem of current distribution as discussed in [34] due to the series-parallel connection on the secondary side.

In [35], the proposed topology addresses the issues discussed in [33, 34]. The transformers were center tapped, each accommodated with their own rectification unit and connected in series thereafter. The center tapping leads to a reduction in turn ratio irrespective of the mode of operation. The series connection forced the current to be the same, which in turn forced the primary side current to be the same. The even distribution of the current on the primary side allows the converter to operate at a higher efficiency despite being at light loads. This makes the converter behave as if it is operating at full load and ensure ZVS operation over the entire range. The reported efficiency was found to be 96.4 % at full load. [36] proposed a multi-port bidirectional system. The system consisted of CLLC resonant converter and an interleaved buck converter. The power flow in each parallel connected stack is controlled independently with the help of the interleaved buck converters. Each stack, therefore, was decoupled. [37] proposed a Partial Parallel Dual Active Bridge Converter (P^2DAB) for high power renewable energy system integration. This topology offered 2 degrees of freedom to control either voltage or power. A similar connection, as discussed in [35], has been utilized to force the current components on the low voltage (LV) side to remain essentially the same. Experimental results indicated that by regulating the phase angles, the converter efficiency can be improved at light loads. Based on this review, two-parent topologies were identified, Dual Active Bridge (DAB) and resonant converter.

For this study, the dual active bridge converter has been chosen due to its ability to provide galvanic isolation, operate at very high efficiency (greater than 99 %), and the ability to incorporate soft-switching without introducing additional passive components in contrast to the resonant topology.

2.5. CONCEPT OF ADAPTIVE MODULARITY

With reference to specifications provided in Table 2.1, the stack current is expected to be,

$$I_{\text{stack}} = \frac{P_{\text{rated}}}{V_{\text{stack}}} = 1.42 \text{ kA}$$

This is an extremely high current on the low-voltage side of the converter. If a single converter was designed to deliver this current, the overall losses especially, the conduction losses will be dominant and converter efficiency would deteriorate. More importantly, due to prolonged operation, the switches on the low voltage side will have a smaller lifetime, and therefore, reliability takes a bigger hit. This is evident from the converter topology review discussed in the previous section. Adopting a modular architecture for the converter utilized in such an application may prove to be a potential solution to achieve this objective. [38] provides an overview of isolated dual active bridge converter for high-frequency link power conversion systems. The authors have emphasized on the typical applications of DAB for high-power link AC-AC Solid State Transformer (SST), DC-DC

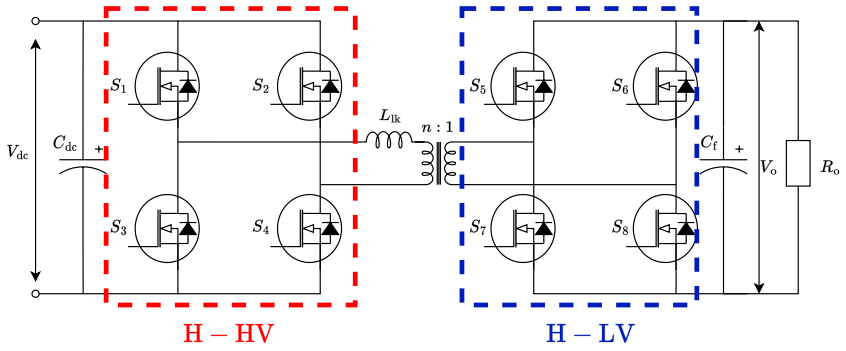

Figure 2.10: Dual Active Bridge Converter.

SST, and Back to Back (BTB) configurations. In this chapter, multiple DAB modules are used as power electronic interfaces between the DC grid and the electrolyzer stacks to handle the high operating current rating, each consisting of two H-bridges as shown in Figure 2.10. Herein, H-HV and H-LV are the HV- and LV-side H-bridges respectively. Three different configurations are considered to redistribute the current on the LV side and ensure that there is minimal stress on the switches, and therefore improve the efficiency of the system.

CONFIGURATION A (FIGURE 2.11)

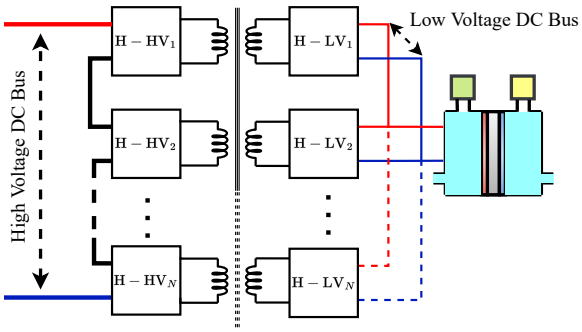

Figure 2.11: Configuration A: Series connected H-HV and parallel connected L-LV bridges for a common electrolyzer stack.

Each DAB module is connected in series on the HV side and in parallel on the LV side. This may be beneficial as the voltage and current rating of individual switches for H-HV and H-LV bridges can be reduced by $\frac{1}{N}$, respectively. This is similar to the topology proposed in [39] that describes DAB systems for MVDC distribution grids.

CONFIGURATION B (FIGURE 2.12)

Each DAB module is connected in parallel to the DC bus on both the HV- and LV- side of the system. While the current rating of individual switches of the H-LV bridges reduces

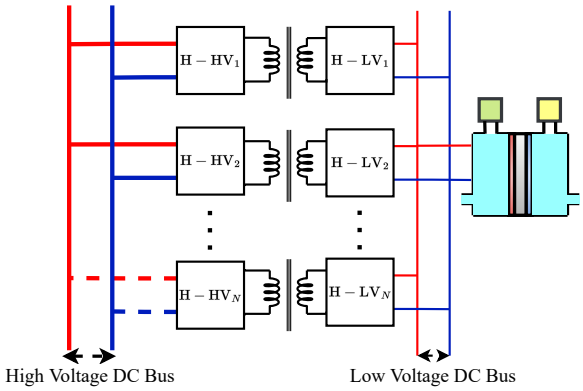

Figure 2.12: Configuration B: Parallel connected H-HV and parallel connected H-LV bridges for a common electrolyzer stack.

by $\frac{1}{N}$, the voltage rating of all H-HV bridge switches must be rated according the dc grid voltage. However, unlike configuration A, each DAB module can be activated or deactivated during operation to route the power efficiently between the electrolyzer and the grid.

CONFIGURATION C (FIGURE 2.13)

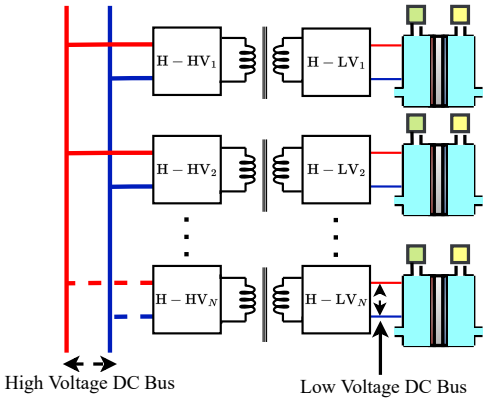

Figure 2.13: Configuration C: Parallel connected H-HV and parallel connected H-LV bridges for a dedicated electrolyzer stack for each DAB module.

Each DAB module is connected to a dedicated electrolyzer stack such that there are N independent systems, each with power rating $\left(\frac{1}{N}\right)^{\text{th}}$ of the rated system power. Depending on the adaptive operation of DAB modules in accordance with the power flow, the IV characteristics of the active stack can be modified, thus influencing the system efficiency.

2.6. SYSTEM ARCHITECTURE

In order to design a conversion system with high efficiency, both converter topology and system architecture need to be discussed. The unification of the electrolyser stack size and working parameters of the electrical power supply serves as the principal aspect of the overall system efficiency and investment value. One can define four main architecture types for electrolysis systems which will be described in the following:

- Direct/Independent Connection
- Series Connection
- Mixed Connection

2.6.1. DIRECT/INDEPENDENT CONNECTION

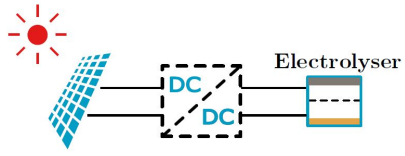

(a) Direct Connection

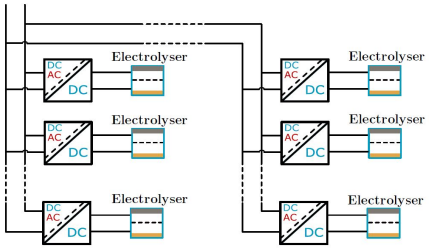

(b) Independent Connection

Figure 2.14: Direct/Independent Connections

This architecture implies that electrolyser cells are directly connected to the electrical energy source, in other words they are independent of one another. In this way, each cell can be controlled to operate at its optimal power and any fault on the electrolyser side would not propagate to other cells. This architecture is appealing for standalone systems with renewable-based electrical energy generation because it allows for operation at the maximum power in all conditions by use of, for example, module level converters for PV panels, see Figure 2.14a [40]. Direct coupling between PV modules and electrolysers without additional conversion stages can be considered, as the lower number of conversion stages and lack of a battery energy storage system BESS, which is popular in standalone systems theoretically leads to higher conversion efficiency and lower system cost [41–43]. The arrangement should be so that the static I-V curve of the water electrolyser should match the maximum power point (MPP) curve of the solar panel configuration [44, 45].

However, control systems for the flow of water and outtake gasses still have to be implemented and experiments show that even if solar-to-hydrogen efficiencies of 8.5 % were recorded, a converter stage with maximum power point tracking (MPPT) algorithm provides better energy efficiency by about 14.5 % [46]. One other way of connecting the individual cells or stack of cells is by a shared DC or AC bus within the plant as shown in Figure 2.14b.

2.6.2. PARALLEL CONNECTION

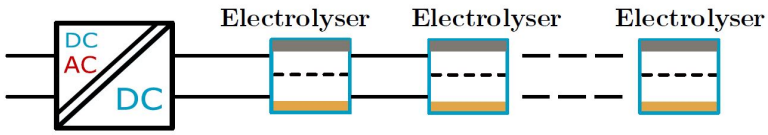

Figure 2.15: Parallel Connection

Studies have pointed out that the selectivity of reaction products for CO_2 electrochemical reduction heavily depends on the cell voltage, thus one of the options for up-scaling an electrolysis system is to connect the electrolysers in parallel as shown in Figure 2.15 [47–49]. In this way the cell voltage and implicitly the electrolysis reaction can be controlled, this connection is analogous to the extension of the electrode surface and essentially linearly increases the production rate. The production rate of a given electrolysis process is given by

$$f = \eta_F \frac{j_{cell} A_{cell}}{zF} \tag{2.26}$$

where f is the production rate (mol s^{-1}) of the electrolysis product, for example, f_{H_2} in the case of water splitting or f_{CO} in the case of CO_2 electrochemical reduction, η_F is the Faraday efficiency of the reaction, j_{cell} is the current density (A cm^{-2}), A_{cell} is the effective cell area (cm^2), z is the number of moles of electrons transferred and F is the Faraday constant (96485 C mol^{-1}).

For the power supply, up-scaling such a system entails the necessity of providing the entire system with a voltage equal to the cell voltage, in the range of 3 V for low-temperature CO_2 electrochemical reduction, and a current intensity proportional to the system power. It is easy to observe that such an architecture is very limited because it quickly leads to unrealistic current requirements for high-power systems (e.g. 3.33 MA for a 10 MW system). The implementation of this connection type is not used in practice due to the low capacity of up-scaling to high power.

2.6.3. SERIES CONNECTION

Stacking up the electrolyser cells in series is one other method of up-scaling, and its essential benefit over the parallel connection is that it can be provided with a higher voltage level, resulting in a lower current intensity value when system power is accounted for, as shown in Figure 2.16. Both power supply and connecting wires' conduction losses are greatly reduced due to the proportionality to the square of the effective current value I^2_{RMS}.

The series connection also has limits as small voltage imbalances that can be observed among a string of series-connected electrolyser cells can add up to large imbalances in a stack with a large number of cells, and as stated in the previous section, the selectivity of the electrochemical reaction is strongly dependent on the cell voltage.

The limiting factor for this architecture is also the gas-pressure equalization within the cells, in the case of alkaline electrolysers [29], and the overall stack voltage which

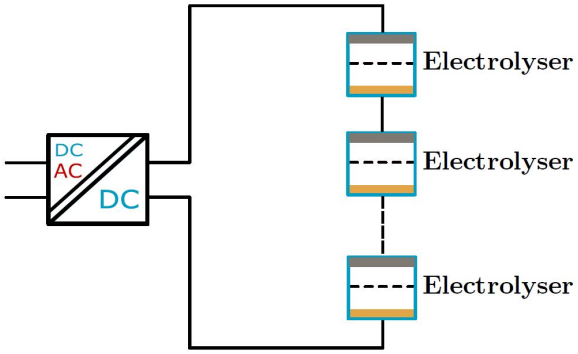

Figure 2.16: Series Connection

should be kept low enough to avoid discharges and the danger of explosions (for hydrogen systems). This architecture is used in the highest power commercial water electrolysers [19, 22, 50, 51]

2.6.4. MIXED CONNECTION

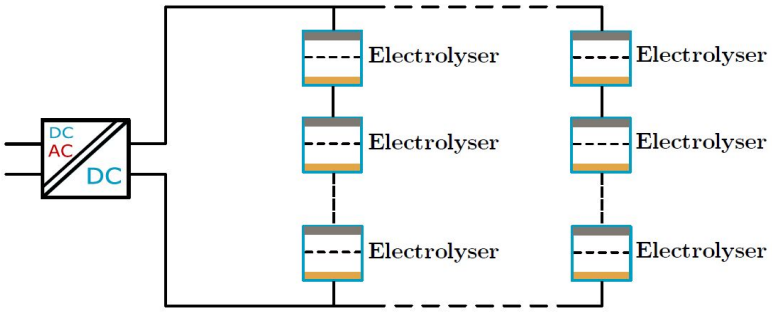

Figure 2.17: Mixed Connection

A combination of the previous architectures should be considered for high-power electrolysis units as shown in Figure 2.17. Connecting multiple strings in parallel allows for higher power systems with a low component count. The supplied current will be higher than what is required for a single series connected stack because of the limiting requirement for stack voltage, but lower than the parallel scheme.

Just like the series connection, this architecture is also limited by the overall stack voltage and input gas-pressure equalization. Modular mixed connection systems have been proposed in the literature, where each module comprised of a stack or series connection of stacks is independently operated by DC-DC converters [52]. This allows for system control strategies such as selective shut-down of modules with the purpose of an efficient system operation under variable power conditions (also known as a load-following operation).

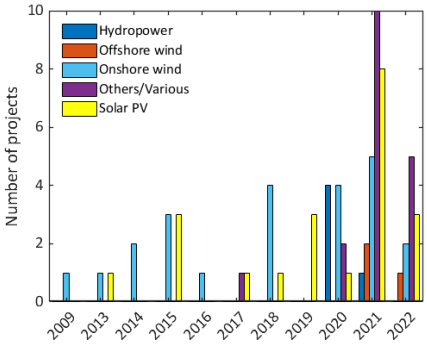

Figure 2.18: Prefered power source to drive large-scale electrolysis projects worldwide. With data from [53].

2.7. OPERATION WITH SOLAR ENERGY

Solar photovoltaic (PV) energy is gaining popularity as the preferred source for powering large-scale electrolysis projects either as a single source or combined with wind power as seen in Figure 2.18.

The solar-to hydrogen (STH) efficiency is a metric to evaluate the amount of irradiance needed to produce hydrogen. It combines the efficiency of the PV system and of the electrolysis system. Figure 2.19a shows the reported STH efficiencies in the last ten years. although there is an increasing trend, there is still a place for improvement. Figure 2.19b shows the STH per coupling type. Battery-assisted and grid-connected systems reach higher efficiencies, possibly because of the continuous operation of the electrolyzer, even at night [54].

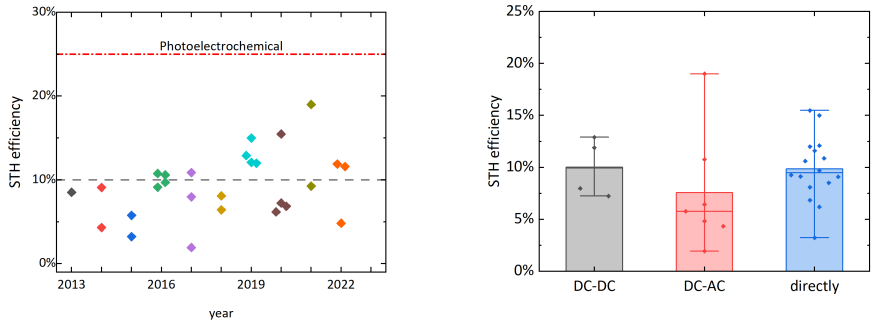

(a) (b)

Figure 2.19: (a) Reported solar-to-hydrogen efficiency per year [54]. The dashed line at 10% indicates the limit at which the projects become economically feasible [55], while the line marked as "Photoelectrochemical" marks the target of the Department of Energy of the United States [56]. Although it is a different technology, it is included as a reference. (b) Solar-to-Hydrogen efficiency per coupling strategy [54]

The electrical response of low-temperature water electrolyzers is extremely fast and

is well suited for variable operation. The evolution of gases and the operating temperature impose the limits on the power ramp that an electrolyzer can withstand. The ramp rate which electrolyzers can tolerate is higher than the ramps of irradiance. Hence irradiance variability is not the bottleneck for solar-powered electrolysis. More importantly, the operation at partial load can raise safety concerns, while slow varying variables, as temperature, have a strong influence on the process efficiency [54].

2.7.1. EFFECT OF SOLAR IRRADIANCE VARIABILITY ON MAXIMUM POWER POINT TRACKING

A maximum power point tracker is an algorithm embedded into a power controller that sets the photovoltaic module's operating point at its maximum power. The *Perturb & Observe* algorithm is a simple, yet effective maximum power point tracking algorithm which is based on the hill-climbing method. The algorithm constantly *perturbs* the module's voltage in small steps and *observes* the power output. Depending on whether this power is higher or lower than the previous step, it will increase or decrease the module's voltage until it swings around the maximum power point. Despite its simplicity, this algorithm is widely implemented in industry.
However, its operation is sensitive to changes in irradiance, causing efficiency losses due to the algorithm tracking away from the maximum power point as seen in Figure 2.20. This happens due to the logic of the algorithm and is independent of the converter controlling the PV module.

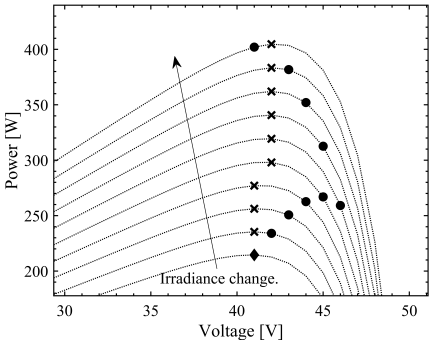

Figure 2.20: Confusion of the Perturb & Observe maximum power point tracking algorithm under changing irradiance. The crosses indicate the maximum power point of the PV module, the solid dots, the steps of P&O and the diamond, the starting point. Note that the algorithm moves the module's voltage away from the maximum power point due to the changing irradiance [57].

The efficiency loss can be related to the variability of solar irradiance by binning the efficiency and irradiance variability. The relation between these two quantities is described with a quadratic polynomial (Eq. 2.27) [57].

$$\bar{\eta}_{MPP} = p_1 \bar{V}^2 + p_2 \bar{V} + p_3 \tag{2.27}$$

Where $\bar{\eta}_{MPP}$ is the average bin efficiency, p_1, p_2, and p_3 are the fitting coefficients and $\bar{V} = \overline{\sigma(\Delta G)}$ is the irradiance variability metric given by the standard deviation of the differences of the solar irradiance G [57].

P&O is described by two operating parameters. The perturbation step (in percentage of the module's open circuit voltage) and the sampling time (indicating how frequent the perturbations will be made). These two parameters influence the efficiency of the algorithm, especially under high variable irradiance conditions [57].

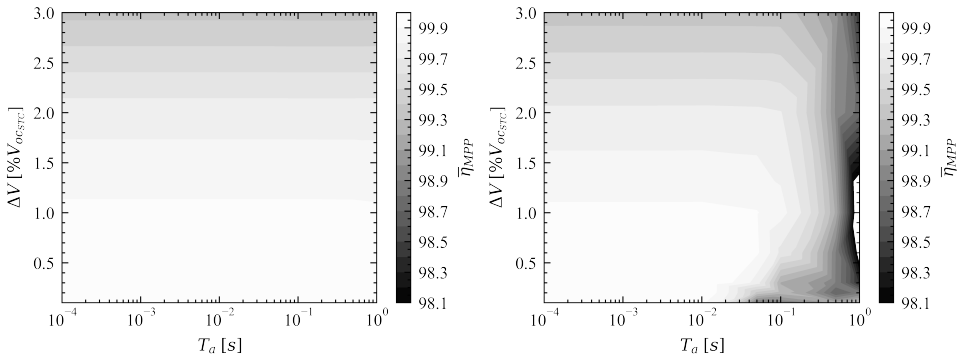

(a) (b)

Figure 2.21: Efficiency loss due to P&O parameters under **(a)** clear skies, and **(b)** variable irradiance [57].

2.7.2. VERY SHORT-TERM PREDICTION OF SOLAR IRRADIANCE

The quick variations in irradiance impose a challenge in the operation of PV systems. To alleviate this, forecasting in the very-short term (a few minutes ahead) appears as a potential solution to these challenges.

Images from the sky provide forecasting models with information about the the clouds: type, location in the sky dome, and, direction and speed in which they move. This information can be incorporated with measured irradiance and artificial intelligence to perform an intra-hour irradiance prediction. One of the main problems with this approach is that the artificial intelligence models tend to smooth the irradiance variations and underperform when the sky conditions change rapidly. One solution is to this is to train several AI models on a specific sky condition. This results in different highly specialized models that require less training data to outperform the single-model version [58].

This solution, requires a pre-processing step that determines the current sky condition and classifies it into five classes. Then the prediction model chooses the appropriate AI model for that particular class [58]. Figure 2.22 shows the block diagram for the pre-processing step. Figure 2.23 shows the structure of the complete model. Each Convolutional Neural Network (CNN) is based on a ResNet50 architecture that receives a three-channel color image plus two extra channels containing the optical flow information (magnitude and direction of pixel movement). A a fully-connected neural network processes the additional data (clear-sky index and the Sun's coordinates in the image) [58].

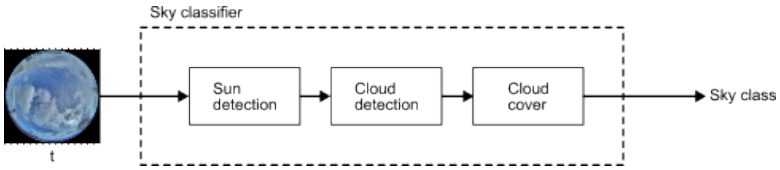

Figure 2.22: Block diagram of the sky classifier. The model detects the location of the Sun in the image and applies a cloud detection algorithm depending on whether the sun is blocked or not. Finally the cloud cover in the image is determined from the detected cloud pixels [58].

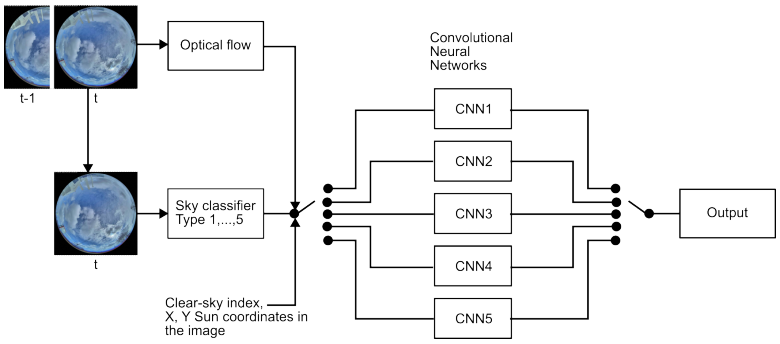

Figure 2.23: Complete structure of the prediction model. The pre-processing steps are the sky classifier and the optical flow, which returns the movement of the pixels between two consecutive images. After the clasification, a particular convolutional neural network trained for specific sky conditions makes the forecasting [58].

This approach leads to a forecasting improvement of up to 20% with respect to the simple persistence model (which assumes constant irradiance throughout the forecasting horizon), and around 10% improvement with respect to the unclassified model as seen in Figure 2.24

2.7.3. OPTIMIZATION OF THE SOLAR-HYDROGEN PLANT

In a stand-alone PV-hydrogen system, the PV provides all the power the electrolyzer needs (and supporting equipment, Balance of Plant). Focusing only on the electrolyzer, there are two main coupling methods. The first is to connect the PV modules to the electrolysis stack without any interface. If the number of electrolyzer cells and PV modules are chosen correctly, the system will operate *close* to the maximum power point of the PV modules, even at changing or low irradiance. The second option is to use a power controller with a maximum power point tracking algorithm. This ensures that the system will operate at the PV module's maximum power point most of the time. The optimization of these systems requires to distribute the PV power into the electrolyzer and the auxiliary equipment. Figure 2.25 shows a schematic of the studied system [59].

The optimization procedure relies on the Particle Swarm Optimization (PSO) algorithm to find the azimuth and tilt of the PV modules and the ratio between the nominal power of the electrolyzer and the PV system (oversize factor). The objective function is either one of three proposed indicators [59]:

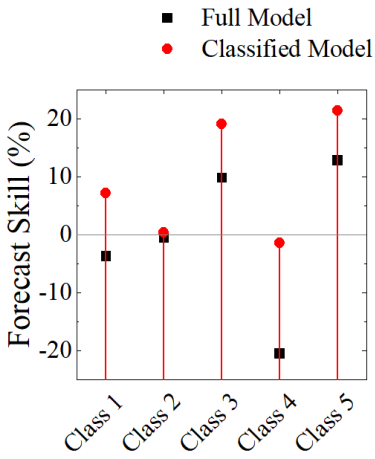

Figure 2.24: Improvement of the prediction (given by the forecast skill) of the classified and unclassified models against the persistence model. positive values indicate that the proposed models outperform the persistence model. Negative values indicate that the persistence model performs better than the proposed models [58]

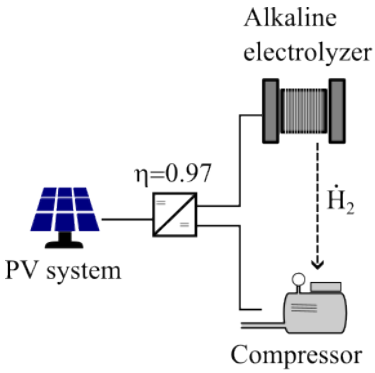

Figure 2.25: Overview of the studied stand-alone solar-hydrogen system [59]

1. Energy consumption (Eq. 2.28). Is a measure of efficiency of the system and relates the produced energy from the PV system $\int_{\text{year}} P_{\text{PV}}$ to the yearly production of hydrogen $\int_{\text{year}} \dot{H}_2$. the units are in kWh/kg_{H_2}.

$$\text{Energy use} = \frac{\int_{\text{year}} P_{\text{PV}}}{\int_{\text{year}} \dot{H}_2} \tag{2.28}$$

2. Wasted energy ((Eq. 2.29). Is a measure of energy that could be produced by the PV system but cannot be used to produce hydrogen as it would exceed the nominal capacity of the electrolyzer, hence, it it curtailed $P_{\text{curtailed}}$, or, it is below the minimum threshold to start the process, so it is unused P_{unused}.

$$\text{Wasted energy} = \frac{\int_{\text{year}} (P_{\text{unused}} + P_{\text{curtailed}})}{\int_{\text{year}} \dot{H}_2} \tag{2.29}$$

3. Levelized Cost of Hydrogen (LCOH) (Eq. 2.30). Represents the cost of hydrgogen along the lifetime of the project. I_t and M_t are the investment and maintenance costs in year t, respectively. r represents the interest rate and H_t the produced hydrogen in year t.

$$LCOH = \frac{\sum_{t=0}^{n} \frac{I_t + M_t}{(1+r)^t}}{\sum \frac{H_t}{(1+r)^t}} \tag{2.30}$$

Figure 2.26 show the orientation of the PV modules to minimize the indicators. Two scenarios were studied, single-sided PV systems (Figure 2.26a) and double-sided (Figure 2.26b). Note that in single-sided systems, the optimal orientation does not coincide with the optimum orientation which maximizes the electricity yield of PV modules. And even more remarkably, the energy consumption is minimized with north-facing modules (even when the system under study is in the Northern hemisphere), with a very large oversize factor (the PV system should be 5 times larger than the hydrogen system). Naturally, cost-wise the system is aligned closer to the optimum PV orientation with smaller systems (an oversize factor slightly above 2.5). This configuration also results in a better use of the electrolyzer as it causes it to operate longer at full load than configuration optimizing energy consumption or wasted energy [59].

2.8. CONCLUSIONS

The presence of low voltage and high current at the stack side is not straightforward to solve from the converter design perspective. This necessitates developing power electronics solutions with the objective of redistributing this current such that the losses are minimized. In this chapter, a simplified model of an alkaline regenerative stack is developed, and the effect of varying certain parameters on its electrical characteristics is discussed. Furthermore, the insights obtained from the same are co-related with the power electronics converter design challenges, operational challenges, and their associated trade-offs with regard to the electrolyzer system. A converter topology review has

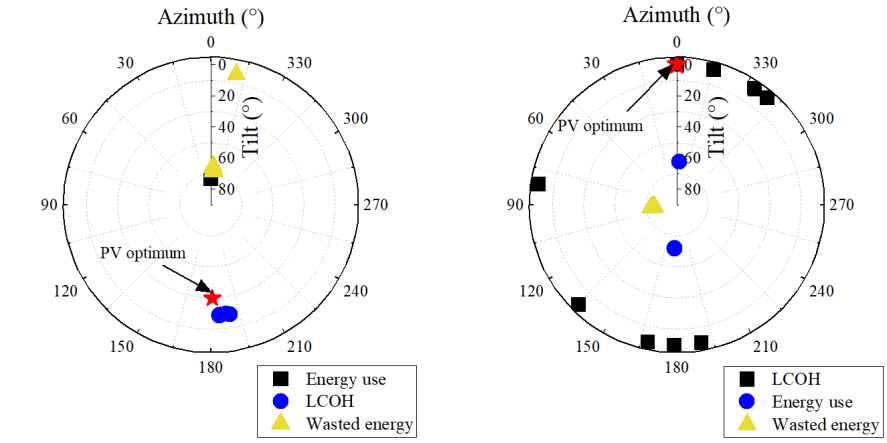

Figure 2.26: Optimized configurations after 10 runs of PSO for (a) Single-sided (All PV modules have the same azimuth and tilt) and (b), double-sided orientation (half of the PV modules share the same tilt but their azimuth is shifted 180°) [59].

been conducted, followed by an introduction to the concept of adaptive modularity for power electronics converters employed for green hydrogen production. Three potential configurations based on the DAB converter are introduced, and the advantages of applying adaptive modularity to these configurations have been discussed. The modular converter configurations can also be influenced by the type of system architecture of the electrolyzer systems. Therefore, various electrolyzer system architectures in the literature were emphasised upon along with their key features, merits, and demerits.

REFERENCES

[1] M. van Economische Zaken en Klimaat, *Klimaatakkoord,* (2019).

[2] E. Commission, *Eu climate strategies and targets,* (2020).

[3] U. Nations, *Paris agreement,* (2016).

[4] A. Government, *Renewables take to the skies, rails and roads,* (2019).

[5] U. N. University, *European trains go down renewable route,* (2017).

[6] McPhy, *Industrial hydrogen: a 20 mw project in the netherlands,* (2020).

[7] C. Pascalau, T. B. Soeiro, N. H. van der Blij, and P. Bauer, *Electrical energy conversion for low temperature electrolysis-challenges and future trends,* in *2021 IEEE 19th International Power Electronics and Motion Control Conference (PEMC)* (IEEE, 2021) pp. 349–356.

[8] N. R. Shriyan, *Modelling of PV-Electrolyzer system for optimum operation*, Master's thesis, Delft University of Technology (2020).

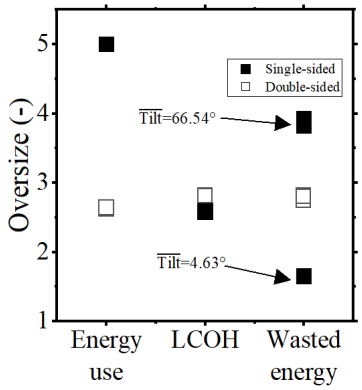

Figure 2.27: Oversize configuration of the single and double-sided systems for the three indicators. $\overline{\text{Tilt}}$ indicate the average tilt of a cluster of results [59].

[9] M. Carmo, D. L. Fritz, J. Mergel, and D. Stolten, *A comprehensive review on pem water electrolysis,* International journal of hydrogen energy **38**, 4901 (2013).

[10] Ø. Ulleberg, *Modeling of advanced alkaline electrolyzers: a system simulation approach,* International journal of hydrogen energy **28**, 21 (2003).

[11] H. Wendt and V. Plzak, *Hydrogen production by water electrolysis/wasserstoffproduktion durch elektrolyse von wasser,* Kerntechnik **56**, 22 (1991).

[12] L. Nuttall, A. Fickett, and W. Titterington, *Hydrogen generation by solid polymer electrolyte water electrolysis,* in *Hydrogen energy* (Springer, 1975) pp. 441–455.

[13] W. Grubb, *Batteries with solid ion exchange electrolytes: I. secondary cells employing metal electrodes,* Journal of the Electrochemical Society **106**, 275 (1959).

[14] W. Grubb, *Ionic migration in ion-exchange membranes,* The Journal of Physical Chemistry **63**, 55 (1959).

[15] W. Dönitz and E. Erdle, *High-temperature electrolysis of water vapor—status of development and perspectives for application,* International Journal of Hydrogen Energy **10**, 291 (1985).

[16] E. Commission, *Innovative solid oxide electrolyser stacks for efficient and reliable hydrogen production,* (2016).

[17] H. Xu, B. Chen, J. Irvine, and M. Ni, *Modeling of ch4-assisted soec for h2o/co2 coelectrolysis,* International Journal of Hydrogen Energy **41**, 21839 (2016).

[18] D. Falcão and A. Pinto, *A review on pem electrolyzer modelling: Guidelines for beginners,* Journal of Cleaner Production **261**, 121184 (2020).

[19] A. Ursúa and P. Sanchis, *Static-dynamic modelling of the electrical behaviour of a commercial advanced alkaline water electrolyser,* International journal of hydrogen energy **37**, 18598 (2012).

[20] N. Gallandat, K. Romanowicz, and A. Züttel, *An analytical model for the electrolyser performance derived from materials parameters,* Journal of Power and Energy Engineering **5**, 34 (2017).

[21] D. Aikens, *Electrochemical methods, fundamentals and applications,* (1983).

[22] J. Koponen, V. Ruuskanen, A. Kosonen, M. Niemelä, and J. Ahola, *Effect of converter topology on the specific energy consumption of alkaline water electrolyzers,* IEEE Transactions on Power Electronics **34**, 6171 (2018).

[23] A. Kosonen, J. Koponen, V. Ruuskanen, M. Niemela, J. Ahola, J. Geisbusch, and P. Kreideweis, *Dynamic behavior emulation of alkaline electrolyzer by power-hardware-in-the-loop,* in *2018 20th European Conference on Power Electronics and Applications (EPE'18 ECCE Europe)* (IEEE, 2018) pp. P–1.

[24] A. S. Tijani, M. A. Ghani, A. A. Rahim, I. K. Muritala, and F. A. B. Mazlan, *Electrochemical characteristics of (pem) electrolyzer under influence of charge transfer coefficient,* international journal of hydrogen energy **44**, 27177 (2019).

[25] C. Rozain and P. Millet, *Electrochemical characterization of polymer electrolyte membrane water electrolysis cells,* Electrochimica Acta **131**, 160 (2014).

[26] B. Endrodi, E. Kecsenovity, A. Samu, F. Darvas, R. Jones, V. Török, A. Danyi, and C. Janáky, *Multilayer electrolyzer stack converts carbon dioxide to gas products at high pressure with high efficiency,* ACS energy letters **4**, 1770 (2019).

[27] J. C. Ganley, *High temperature and pressure alkaline electrolysis,* International journal of hydrogen energy **34**, 3604 (2009).

[28] *Cottrell equation,* https://en.wikipedia.org/wiki/Cottrell_equation, accessed: 2022-07-15.

[29] R. Pittini, Z. Zhang, and M. A. Andersen, *Isolated full bridge boost dc-dc converter designed for bidirectional operation of fuel cells/electrolyzer cells in grid-tie applications,* in *2013 15th European Conference on Power Electronics and Applications (EPE)* (IEEE, 2013) pp. 1–10.

[30] A. Brisse, J. Schefold, C. Stoots, and J. O'Brien, *Electrolysis using fuel cell technology,* in *Innovations in fuel cell technologies* (Royal Society of Chemistry, 2010) pp. 263–286.

[31] N. Mohan, T. M. Undeland, and W. P. Robbins, *Power electronics: converters, applications, and design* (John wiley & sons, 2003).

[32] L. Zubieta and G. Panza, *A wide input voltage and high efficiency dc-dc converter for fuel cell applications,* in *Twentieth Annual IEEE Applied Power Electronics Conference and Exposition, 2005. APEC 2005.*, Vol. 1 (IEEE, 2005) pp. 85–89.

[33] S.-S. Lee, S.-W. Choi, and G.-W. Moon, *High-efficiency active-clamp forward converter with transient current build-up (tcb) zvs technique,* IEEE Transactions on Industrial Electronics **54**, 310 (2007).

[34] C. Liu, A. Johnson, and J.-S. Lai, *A novel three-phase high-power soft-switched dc/dc converter for low-voltage fuel cell applications,* IEEE Transactions on Industry Applications **41**, 1691 (2005).

[35] K. Sternberg and H. Gao, *A new dc/dc converter for solid oxide fuel cell powered residential systems,* in *2008 34th Annual Conference of IEEE Industrial Electronics* (IEEE, 2008) pp. 2273–2277.

[36] X. Lin, K. Sun, J. Lin, Z. Zhang, and W. Kong, *A multi-port bidirectional power conversion system for reversible solid oxide fuel cell applications,* in *2018 International Power Electronics Conference (IPEC-Niigata 2018-ECCE Asia)* (IEEE, 2018) pp. 3460–3465.

[37] Z. Zhang, K. Tomas-Manez, Y. Xiao, and M. A. Andersen, *High voltage gain dual active bridge converter with an extended operation range for renewable energy systems,* in *2018 IEEE Applied Power Electronics Conference and Exposition (APEC)* (IEEE, 2018) pp. 1865–1870.

[38] B. Zhao, Q. Song, W. Liu, and Y. Sun, *Overview of dual-active-bridge isolated bidirectional dc–dc converter for high-frequency-link power-conversion system,* IEEE Transactions on power electronics **29**, 4091 (2013).

[39] M. Stieneker and R. W. De Doncker, *Dual-active bridge dc-dc converter systems for medium-voltage dc distribution grids,* in *2015 IEEE 13th Brazilian Power Electronics Conference and 1st Southern Power Electronics Conference (COBEP/SPEC)* (IEEE, 2015) pp. 1–6.

[40] M. Kasper, D. Bortis, and J. W. Kolar, *Classification and comparative evaluation of pv panel-integrated dc–dc converter concepts,* IEEE Transactions on Power Electronics **29**, 2511 (2013).

[41] N. A. Kelly, T. L. Gibson, and D. B. Ouwerkerk, *A solar-powered, high-efficiency hydrogen fueling system using high-pressure electrolysis of water: Design and initial results,* International journal of hydrogen energy **33**, 2747 (2008).

[42] L. Arriaga, W. Martinez, U. Cano, and H. Blud, *Direct coupling of a solar-hydrogen system in mexico,* International journal of hydrogen energy **32**, 2247 (2007).

[43] R. García-Valverde, N. Espinosa, and A. Urbina, *Optimized method for photovoltaic-water electrolyser direct coupling,* international journal of hydrogen energy **36**, 10574 (2011).

[44] M. Zhou and Y. Liu, *Theoretical study on direct coupling of a pv array to a pem electrolyser,* in *2013 International Conference on Materials for Renewable Energy and Environment*, Vol. 1 (IEEE, 2013) pp. 52–56.

[45] F. Sayedin, A. Maroufmashat, S. Al-Adwani, S. S. Khavas, A. Elkamel, and M. Fowler, *Evolutionary optimization approaches for direct coupling photovoltaic-electrolyzer systems,* in *2015 International Conference on Industrial Engineering and Operations Management (IEOM)* (IEEE, 2015) pp. 1–8.

[46] G. M. Sriramagiri, N. Ahmed, K. D. Dobson, and S. S. Hegedus, *Modeling and analysis of photovoltaic electrochemical system using module-level power electronics,* in *2017 IEEE 44th Photovoltaic Specialist Conference (PVSC)* (IEEE, 2017) pp. 658–662.

[47] R. Kortlever, J. Shen, K. J. P. Schouten, F. Calle-Vallejo, and M. T. Koper, *Catalysts and reaction pathways for the electrochemical reduction of carbon dioxide,* The journal of physical chemistry letters **6**, 4073 (2015).

[48] A. R. Morrison, V. van Beusekom, M. Ramdin, L. J. van den Broeke, T. J. Vlugt, and W. de Jong, *Modeling the electrochemical conversion of carbon dioxide to formic acid or formate at elevated pressures,* Journal of The Electrochemical Society **166**, E77 (2019).

[49] D. Bohra, I. Ledezma-Yanez, G. Li, W. de Jong, E. A. Pidko, and W. A. Smith, *Lateral adsorbate interactions inhibit hcoo- while promoting co selectivity for co2 electrocatalysis on silver,* Angewandte Chemie **131**, 1359 (2019).

[50] A. Ursúa, P. Sanchis, and L. Marroyo, *Renewable Hydrogen Technologies*, edited by L. M. Gandía, G. Arzamendi, and P. M. Diguez (Elsevier, 2013) pp. 333–360.

[51] J. Solanki, N. Fröhleke, and J. Böcker, *Implementation of hybrid filter for 12-pulse thyristor rectifier supplying high-current variable-voltage dc load,* IEEE Transactions on Industrial Electronics **62**, 4691 (2015).

[52] B. Yodwong, D. Guilbert, M. Phattanasak, W. Kaewmanee, M. Hinaje, and G. Vitale, *Ac-dc converters for electrolyzer applications: State of the art and future challenges,* Electronics **9**, 912 (2020).

[53] International Energy Agency, *IEA projects database,* .

[54] V. Martinez Lopez, H. Ziar, J. Haverkort, M. Zeman, and O. Isabella, *Dynamic operation of water electrolyzers: A review for applications in photovoltaic systems integration,* Renewable and Sustainable Energy Reviews **accepted for publication** (2023).

[55] Argonne National Laboratory, *Basic research needs for the hydrogen economy,* (2003).

[56] Office of energy efficiency & Renewable energy, *Hydrogen and fuel cell technologies office multi-year research, development and demonstration plan,* (2014).

[57] V. Martinez Lopez, U. Žindžiūtė, H. Ziar, M. Zeman, and O. Isabella, *Study on the effect of irradiance variability on the efficiency of the perturb-and-observe maximum power point tracking algorithm,* energies **15**, 7562 (2022).

[58] V. Martinez Lopez, G. van Urk, P. Doodkorte, M. Zeman, O. Isabella, and H. Ziar, *Using sky-classification to improve the short-term prediction of irradiance with sky images and convolutional neural networks,* **submitted** ().

[59] V. Martinez Lopez, H. Ziar, M. Zeman, and O. Isabella, *Maximization of pv energy use and performance analysis of a stand-alone pv-hydrogen system,* **submitted** ().

3

WP-3: Design Rules for Intelligent Power-Electronic Components for Controlling Power Quality in Urban Networks

3.1. Introduction

GRID-connected power electronics converters are getting more attention due to climate change, renewable energy sources integration, and fossil-free transportation [1]. The extensive interconnection of power electronics-based systems into power grids is affecting the reliability of the system. Modular multilevel converter (MMC) is an attractive topology among others for medium to high voltage applications [2]. MMC is a promising candidate due to its modularity, scalability, high efficiency, and superior harmonic performance [3]. However, higher modularity consequently increases the number of components in the system, thereby influencing the risk of failure [4]. Therefore, the cost-effective design for reliability by considering the trade-off between modularity and redundancy is important [5].

For the MMC design, reliability and cost-based methods by only considering redundancy are reported in [6–9]. In [6], the cost-based model of the MMC with two redundancy strategies is evaluated, and it is presented that standby redundancy has a lower cost than active redundancy. Authors in [7] present an optimization method by considering the cost and redundancy aspects of the MMC with hybrid sub-modules (SMs). In [8], a method is proposed that provides reliability indices to plan periodic preventive maintenance for the MMC in off-shore applications. In [9], three converter topologies, including 2-level, 3-level neutral-point-clamped (NPC) and MMC with fixed switch volt-

Table 3.1: Comparison of the Existing Literature and Proposed Study for MMC Design

Reference	Mod†	Red‡	Cost	Varying DC link vol	Varying loading
[15]	✓		✓		✓
[16]	✓	✓		✓	
[9]		✓	✓	✓	✓
[18]	✓	✓	✓		
[6–8]		✓	✓		
[10–14]		✓			
Current study	✓	✓	✓	✓	✓

† Modularity ‡ Redundancy

age rating of 4.5 kV are compared for Medium Voltage (MV) applications. Analysis of [9] shows that using 3-level NPC is the most economical when the rated current is below 400 A and DC link voltage is below 56 kV. If the rated current is in the range of 500 A-700 A and DC link voltage is above 46 kV, MMC is the most cost-efficient choice. Likewise, for the current rated above 700 A, regardless of DC link voltage, MMC is the most cost-efficient converter. The design of the MMC that only focuses on redundancy are well-explored in [10–14], where the system reliability is improved by applying different redundancy strategies. For instance, in [11], a redundancy strategy is proposed where the redundant SMs can be shared among all arms. It is presented that with this redundancy strategy, the number of required redundant SM is decreased by 33 % compared to the conventional redundancy strategies.

Modularity (switch voltage rating) is another factor in the MMC that can play an important role in the reliability and cost (initial investment and operational loss) aspects. Few works [15–18] have reported on the design of the MMC by considering modularity aspects of the MMC. In [15], a mission profile method is proposed to design the 17 MW 28 kV DC link MMC with the focus on modularity to suggest that SM with switches of 3.3 kV voltage rating are the most reliable and cost-efficient choice as compared to other market available ratings. The impact of redundancy is considered in [16], and it is suggested that 3.3 kV switch is the optimal choice for line-to-line AC side voltages between 22 kV and 58 kV in an MV cascaded H-bridge AC-DC converter. In [17], the reliability of the MMC by applying individual insulated-gate bipolar transistor (IGBT) SM using Hipak style IGBTs, and series valve SM using press-pack IGBT are compared. It is shown that using Hipak style IGBTs has the lowest conduction losses, while for the first few operational years, presspack IGBTs are more effective in preventing the arm's voltage from decreasing, and the need for installing redundant SMs decreases. [18] compares the semiconductor with different rated voltages to find the optimum choice based on SM utilization and losses for high-voltage direct current (HVDC) applications. Authors conclude that HVDC in the power range below 900 MW, 4.5 kV switch is optimal. For the power range between 900 and 1000 MW, both switches with rating voltage of 4.5 kV and 6.5 kV have similar performance, while the switch with a rating voltage of 6.5 kV is optimal for power range above 1000 MW.

Table 3.1 summarizes and compares the existing literature with the proposed method

in this study. In this chapter, both concepts of redundancy and modularity as two aspects of reliability in the MMC are combined to suggest the optimum voltage rating of the switch. Concerning costs, the insights of [15] are extended by considering the costs associated with redundancy and its corresponding sensitivity to different system parameters such as DC link voltage, average converter loading, required lifetime, and energy price. This chapter aims to quantitatively establish the trade-off between the impact of higher modularity on converter reliability corresponding to the redundancy costs for the given lifetime requirements while considering the operational efficiency. The key contributions of this study are as follows:

- Quantify the MMC's trade-off between modularity and redundancy by varying the submodule switch rating and suggesting the optimal number of levels for the given DC link voltage and operating power considering the capital cost, efficiency, and reliability.
- Derive a generalized insight on selecting the optimal switch rating considering the above trade-off with varying DC link voltage, power rating, average loading, required lifetime, failure rate (FR), components cost, and energy price.
- It also investigates the influence of using two different methodologies (Military Handbook (MIL-HDBK) and FIDES) for calculating the FR of components and the effect of various current ratings.

The rest of the chapter is organized as follows. In Section 3.2, the characteristics of the system and the method for analyzing the MMC reliability are given. Section 3.3 defines a case study and evaluates the system's cost, reliability, and efficiency. Sensitivity analysis is carried out in Section 3.4. In Section 3.5, the general application proposed in this chapter is recommended, and the conclusions are given in Section 3.6.

3.2. SYSTEM DESCRIPTION AND RELIABILITY DESIGN

This section provides a system description and the methodology for evaluating the reliability.

3.2.1. MODULARITY DESIGN

The general configuration of the MMC with half-bridge (HB) SM is presented in Figure 3.1. MMC is composed of three phases, and each phase has two arms. Each arm has a number of SMs connected in series with arm inductance. In this study, as an example, the considered MMC system has rated power (S_n) of 10 MVA with line voltage (V_g) of 8.16 kV. The DC link voltage (V_{dc}) can be estimated by [16]:

$$V_{dc} = \frac{2\sqrt{2} \times V_s}{\sqrt{3} \times m} \tag{3.1}$$

where m is the modulation index and it is equal to 0.96, V_s is the RMS of line-to-line voltage equal to $\sqrt{3}/\sqrt{2}\ V_g$. The minimum number of required SMs (N_{min}) in each arm depends on the selected power switch rating. Besides this, the maximum value of SM

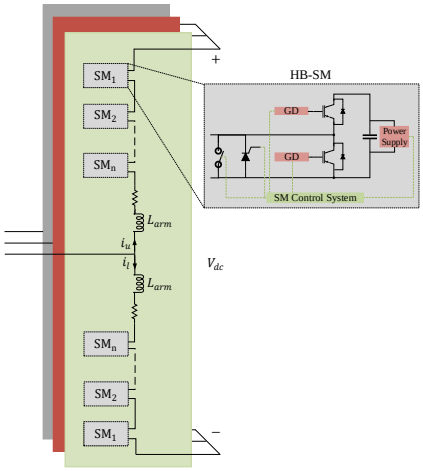

Figure 3.1: Illustration of an MMC with half bridge sub-modules.

capacitors voltage ripple $k_{\max}$ needs to be considered (which in this study is equal to 10 %). Hence, $N_{\min}$ is defined as (3.2) [19]:

$$N_{\min} = \text{Ceil}\left[\frac{k_{\max} \times V_{\text{dc}}}{S_{\text{f}} \times V_{\text{IGBT}}}\right] \tag{3.2}$$

where Ceil (x) function returns the smallest integer that is greater than or equal to x, S_{f} is the safety factor of IGBT that can be determined based on the voltage limits for steady-state operation of MMC, V_{IGBT} is the IGBT blocking voltage. In this work, the safety factor is equal to 0.65, which is in the range of maximum steady state voltage of IGBT [18]. A design element that plays a crucial role in the cost, reliability, and operation of MMC is the SM capacitor. The time-average stored energy and peak value of capacitor voltage are needed to determine the SM's capacitor. According to [19], the required capacitor is given by:

$$C_{\text{SM}} = \frac{N_{\min} \times S_{\text{n}} \times W_{\text{MMC}}}{3(k_{\max} V_{\text{dc}})^2} \tag{3.3}$$

where W_{MMC} is the required energy storage per MVA that is approximately 40 kJ/MVA as defined in [20].

The operating switching frequency (f_{sw}) is chosen in this study such that the effective frequency ($f_{\text{eff}} = N_{\min} \times f_{\text{sw}} \approx 3$ kHz) is constant for the chosen switch rating with the given DC link voltage. This ensures that the harmonic performance of the designed converter is compliant with IEEE 519 with similar power quality for the same arm/filter inductance when different switch ratings and hence the number of levels are selected [21]. Correspondingly, the varying switching and conduction losses for different operating frequencies and the number of levels can be calculated while ensuring that harmonic performance is the same for the given DC link voltage. Table 3.2 summarizes the number

of SMs per arm, SM capacitance, and switching frequency which are all defined based on the withstand voltage of the IGBT module (V_{IGBT}).

Table 3.2: MMC PARAMETERS FOR FIVE DIFFERENT SWITCHES RATING

V_{IGBT} (kV)	V_{dc} (kV) (3.1)	N_{min} (3.2)	f_{sw} (Hz)	C_{SM} (mF) (3.3)	$V_{\text{SM,av}}$ (kV) (3.4)	$S_{\text{f,act}}$ (3.5)
1.2	17	24	125	9.2	0.71	0.650
1.7	17	17	177	6.5	1.00	0.647
3.3	17	9	334	3.4	1.89	0.629
4.5	17	7	429	2.7	2.43	0.594
6.5	17	5	600	1.9	3.40	0.575

Herein, N_{min} is given by (3.2) and the average operating SM voltage ($V_{\text{SM,ave}}$) is given by (3.4).

$$V_{\text{SM,ave}} = \frac{V_{\text{dc}}}{N_{\text{min}}} \tag{3.4}$$

Consequently, the actual operating safety factor ($S_{\text{f,act}}$) associated with maximum SM voltage is given by (3.5),

$$S_{\text{f,act}} = \frac{k_{\text{max}} V_{\text{SM,ave}}}{V_{\text{IGBT}}} \tag{3.5}$$

As observed, $S_{\text{f,act}}$ is closer to the initial design value S_{f} for lower switch rating due to the impact of ceiling function in (3.2). Consequently, it results in a slightly lower switch utilization and SM FR with higher switch ratings. This effect is reduced when a second ceiling function is applied with redundancy requirements for the given B_{10} lifetime, as discussed in the subsequent section. Furthermore, the difference in switch utilization in trade-off with reliability is further reduced for higher DC link voltages as shown in Figure 3.2.

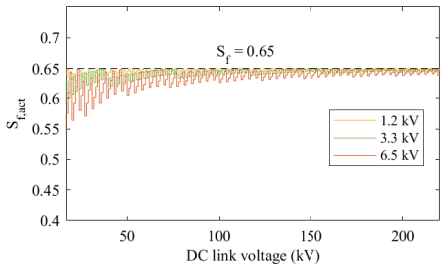

Figure 3.2: The actual safety factor value with varying DC link voltage.

3.2.2. RELIABILITY DESIGN

For reliability analysis of MMC, the FR of the components within the MMC needs to be evaluated. Also, redundancy as a fault-tolerant strategy is applied to increase the

MMC reliability [22]. The following scrutinizes the FR of power components and the redundancy effect.

FR Calculation

In MMC, SMs construct the arms, and its configuration is shown in Figure 3.1. The SM is composed of two IGBTs, a capacitor bank, and auxiliary components [10]. The FR of the switches and capacitor can be calculated by using equations from the MIL-HDBK [23] as (3.6) and (3.9).

$$\lambda_{\text{MIL-IGBT}} = \lambda_{\text{base-IGBT}} \pi_{\text{T}} \pi_{\text{S}} \pi_{\text{A}} \pi_{\text{R}} \pi_{\text{E}} \tag{3.6}$$

where $\lambda_{\text{base-IGBT}}$ is the base FR of IGBT equals to 100 FIT [6]; π_{T} is the temperature factor calculated as (3.7); π_{S} is the factor for voltage stress formulated as (3.8); π_{A} stands for the application factor; π_{R} defines the power rating factor, and π_{E} is the environmental factor [6].

$$\pi_{\text{T}} = exp[-2114 \times [\frac{1}{T_{\text{j}} + 273} - \frac{1}{298}]] \tag{3.7}$$

$$\pi_{\text{S}} = 0.045 \times exp[3.1 \frac{V_{\text{applied}}}{V_{\text{rated}}}] \tag{3.8}$$

where T_{j} is the junction temperature, V_{applied} and V_{rated} are the actual and nominal voltage across the IGBT, respectively.

$$\lambda_{\text{MIL-Cap}} = \lambda_{\text{base-Cap}} \pi_{\text{T}} \pi_{\text{V}} \pi_{\text{SR}} \pi_{\text{Q}} \pi_{\text{E}} \pi_{\text{C}} \tag{3.9}$$

where $\lambda_{\text{base-Cap}}$ is the base FR for film capacitor that is equal to 100 FIT [6]; π_{SR} defines the influencing factor of the series resistance of the capacitor; π_{Q} is the quality coefficient; π_{E} stands for environmental factor; π_{C} is the capacitance coefficient, π_{V} is the voltage stress factor calculated as (3.10), and π_T is the temperature factor formulated as (3.11) [6].

$$\pi_V = [\frac{V_{\text{operating}}}{0.6 \times V_{\text{rated}}}]^5 + 1 \tag{3.10}$$

$$\pi_T = exp[\frac{-0.15}{8.617 \times 10^{-5}} [\frac{1}{T_{\text{j}} + 273} - \frac{1}{298}]] \tag{3.11}$$

where T_{j} is the ambient temperature, which depends on the loading of the converter. In this study, it is assumed if the MMC is not operating (0% loading), the junction temperature of the capacitor and IGBT is equal to the ambient temperature (25^o C) and If it operates at full load (100% loading), the junction temperature is 100^o C. So, the junction temperature can be estimated at any chosen loading. $V_{\text{operating}}$ and V_{rated} are the actual and nominal voltage across the capacitor, respectively.

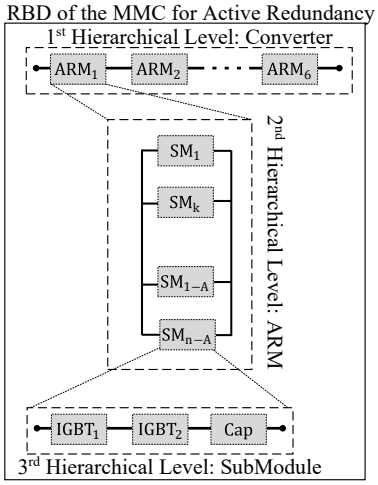

Figure 3.3: RBD model of MMC under active redundancy.

REDUNDANCY EVALUATION

Redundancy as a fault-tolerant strategy is applied to have a normal post-fault operation without degradation [24]. Different redundancy strategies are explored in [10, 20] and the optimal choice depends on many factors such as efficiency, dynamics, and economics. This chapter applies the fixed-level active redundancy strategy [6, 9, 16], and the reliability block diagram (RBD) of MMC with this redundancy is presented in Figure 3.3. In this redundancy strategy, the number of operating SMs within the arm always equals N_{min}. However, in this operating mode, all the SMs (n) are energized, but the triggering signal is only sent to random N_{min} SMs. Hence, all the SMs take turns operating. In this redundancy strategy, triggered SMs could be either original or redundant [16]. As it is shown in Figure 3.3, in fixed-level active redundancy operational state, if N_{red} = n-N_{min} is the number of redundant SMs in each arm, the reliability of the arm can be calculated by applying k-out-of-n given by (3.12) [25].

$$R_{\text{arm}}(t) = \sum_{N_{\text{min}}}^{n} C_n^{N_{\text{min}}} R(t)^{N_{\text{min}}} (1 - R(t))^{n - N_{\text{min}}} \tag{3.12}$$

$$R(t) = e^{-\lambda_{\text{SM}} t} \tag{3.13}$$

$$\lambda_{\text{SM}} = 2 \times \lambda_{\text{MIL-IGBT}} + \lambda_{\text{MIL-Cap}} \tag{3.14}$$

where λ_{SM} is failure of the SM with N_{min} operational SM. For calculating the MMC reliability, since there are six arms, the MMC's reliability is formulated as (3.15)

$$R_{\text{MMC}}(t) = (R_{\text{arm}}(t))^6. \tag{3.15}$$

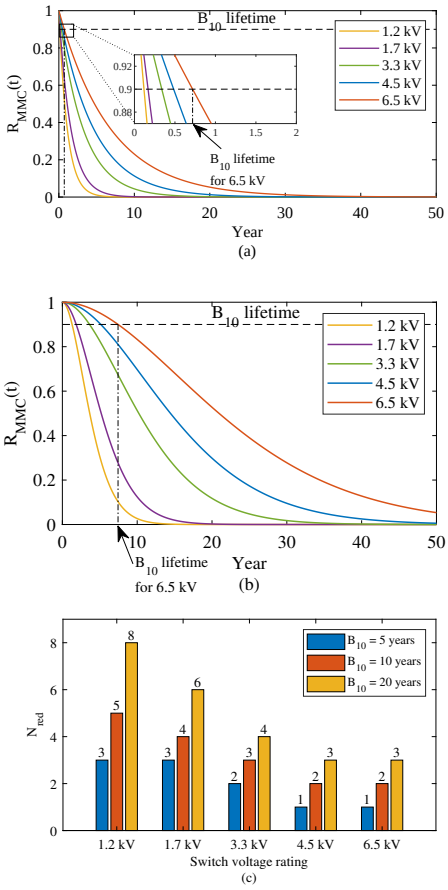

Figure 3.4: Reliability results of 10 MW 17 kV DC link MMC with 57% loading, (a) reliability output for different switch voltage rating with no redundancy, (b) reliability output for different switch voltage rating with one redundant SM in each arm, and (c) number of required redundant SM in each arm to meet B_{10} lifetime requirement of 10 years.

RELIABILITY INDEX

In this study, the percentage of the lifetime B_α is used, which determines what percentage of devices fail at the time as (3.16):

$$F_{\text{MMC}}(B_\alpha) = 1 - R_{\text{MMC}}(B_\alpha) = \frac{\alpha}{100} \tag{3.16}$$

where unreliability function F_{MMC} represents the proportion of population failure. B_{10} lifetime is expressed as the required time to reach 90% of the system's reliability (or 10% of devices fails). Hence, the number of redundant SMs is selected in the design process to reach the required B_{10} lifetime. Table 3.3 shows the B_{10} lifetime of the MMC without redundancy and having one redundant SM in each arm with different switch ratings (obtained from Figure 3.4 (a) and (b) respectively). According to [6, 9, 26, 27], the required

Table 3.3: OBTAINED B_{10} LIFETIME IN YEARS (FIGURE 3.4 (A) AND (B)) FOR 10 MW 17 KV DC LINK MMC WITH DIFFERENT SWITCH RATINGS

Switch ratings		1.2 kV	1.7 kV	3.3 kV	4.5 kV	6.5 kV
B_{10} lifetime	No red	0.12	0.17	0.34	0.48	0.72
	One red	1.31	1.85	3.63	5.14	7.44

lifetime of power electronic systems can vary from 2 years to more than 30 years. Still, the necessary lifetime in most applications falls between 5 to 20 years. Hence, this work considers B_{10} lifetime of 10 years as the reliability index for determining the number of redundant SMs in each arm. Additionally, the sensitivity analysis will be carried out in the case if the required B_{10} lifetime is 5 and 20 years.

Figure 3.4 (a) and (b) show the reliability of the MMC with different switch voltage ratings at 57% loading with no redundancy and only one redundant SM in each arm, respectively. It can be seen from Figure 3.4 (a) and (b) that the inclusion of one redundant SM in the MMC with a higher switch rating improves the reliability much more than the case where a switch with a lower rating is used. However, it is essential to remember that the cost of one redundant SM, for example, for a 6.5 kV switch is higher than a 1.2 kV switch. Hence, there is a trade-off between modularity, redundancy, and cost of the MMC. The MMC's B_{10} lifetime without redundancy and one redundant SM in each arm, as shown in Table 3.3, is less than 10 years. In order to reach the required lifetime of 10 years, more redundant SMs are needed. Figure 3.4 (c) shows the number of redundant SMs required in each arm for the MMC with various switch voltage ratings to meet the 10-year lifetime requirement at 57% loading.

3.3. CASE-STUDIES FOR COST, RELIABILITY, AND EFFICIENCY-BASED OPTIMAL SWITCH SELECTION

With respect to the total cost of the MMC, the capital investment (CI) and operational losses are considered, which are explained in the following.

3.3.1. CAPITAL INVESTMENT

Major components' costs are considered for calculating the CI of the MMC. The dominant components for consideration in CI are power electronics components (semiconductors, control system, power supply) and capacitor cost. Hence, the estimated CI of the power electronics components CI_{PE} is formulated as follows [15]:

$$CI_{\text{PE}} = K_{\text{PE}} N_{\text{semi}} V_{\text{IGBT}} I_{\text{nominal}} \tag{3.17}$$

where I_{nominal} is the nominal or rated current of the IGBT, which in this study is calculated and equals to 480 A, N_{semi} is the total number of IGBT switches in the MMC that is equal to $N_{\text{semi}} = 6 \times 2 \times n$, K_{PE} is the estimated price of installed power that is equal to 3.5€/kVA [28]. The estimated CI of capacitance (CI_{Cap}) can also be calculated from (3.18) - (3.20):

$$CI_{\text{Cap}} = K_{\text{Cap}} E_{\text{Cap}} \tag{3.18}$$

$$E_{\text{Cap}} = 6 \times n \times E_{\text{Cell}} \tag{3.19}$$

$$E_{\text{Cell}} = \frac{1}{2} C_{\text{SM}} V_{\text{SM}}^2 \tag{3.20}$$

where K_{Cap} is the estimated price of the installed capacitor equal to 150 €/kJ. Hence, the CI of the MMC can be estimated by adding the CI of installed capacitance and power electronics switches. In Figure 3.5 (a), the CI of the MMC with different switch ratings for varying DC link voltage at 57% loading is presented. As shown in Figure 3.5 (a), switch rating of 1.2 kV is the most economical option from the only CI point of view throughout the varying DC link voltage. The normalized price can be obtained from (3.21).

$$\text{Normalized CI}(/\,€\text{kVA}) = \frac{CI_{\text{total}}}{S_{\text{n}}}, (S_n \text{ in kVA}). \tag{3.21}$$

As mentioned in section 3.2, redundancy is applied to increase the MMC reliability with various modularity (Figure 3.4 (b)). However, the cost of using redundancy and CI of the MMC differs for different switch ratings; hence, cost aspects are a determining factor in selecting the cost-efficient switch rating while the reliability requirements are met. Figure 3.5 (b) presents the ratio of redundancy costs concerning the total CI of the MMC. As shown from Figure 3.5 (b), applying redundancy has a lower price for higher DC link voltage ranges, while it is more costly for lower DC link voltage ranges. Also, it can be realized that the cost of applying redundancy for the MMC with higher switch voltage rating is more.

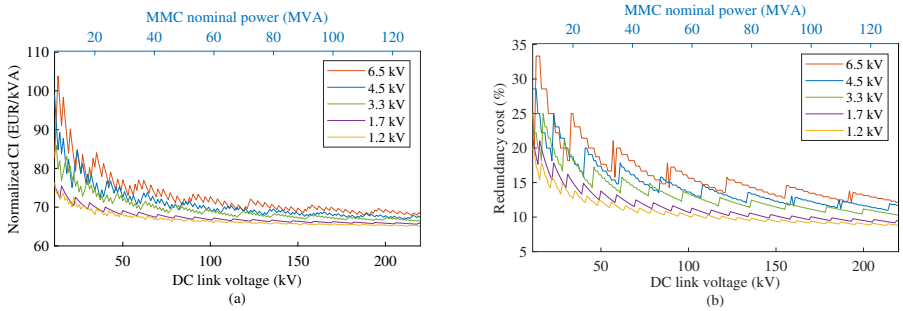

Figure 3.5: Cost results of the MMC with 57% loading, (a) normalized CI of the MMC with different switch voltage rating, (b) redundancy percentage of total CI with B_{10} = 10 years.

3.3.2. Operational Losses

The model developed in [29] is applied to obtain the MMC's operational efficiency with various modularity levels. The physics-based methodology explained in [16] is used to estimate the switching and conduction losses of IGBTs. Also, switching and conduction

losses are evaluated for varying loading. For calculating the annual energy losses (E_l) with different modularity levels, (3.22) is applied as follows:

$$E_l = \int (100 - \eta(t_i)) \times P_{\text{MMC}} \tag{3.22}$$

where $\eta(t_i)$ is the efficiency of the MMC at time t_i and P_{MMC} is the MMC rated power in MW.

3.3.3. CASE STUDY FOR OPERATIONAL LOSSES

Figure 3.6 (a) and (b) show the histogram of two Mission Profiles (MPs) used in this study based on the hourly data adapted from [30]. The average power demand (P_{ave}) of MP I and MP II is 38 % and 57 %, respectively. Figure 3.7 presents the cumulative yearly energy

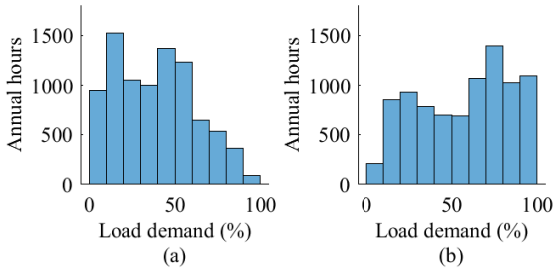

Figure 3.6: Histogram of hourly annual power demand for (a) MP I and (b) MP II.

losses for MMC with different switch ratings according to the daily power demand for two cases shown in Figure 3.6.

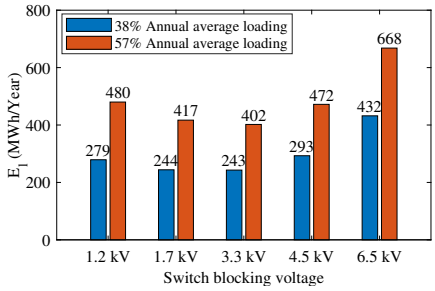

Figure 3.7: Cumulative yearly energy losses E_l for 10 MW 17 kV MMC.

Likewise, these calculations can be repeated for varying DC link voltage other than 17 kV considered. For this evaluation, the phase current is kept constant, and the DC link voltage is changing (as well as the rated power of the MMC). Since the rated current is kept constant, the same switch rating with the same character can be applied, but the number of levels, operational losses, reliability, and CI will change. In Figure 3.8, the conduction and switching losses of the MMC are presented. Switching loss is dominant for

low DC link voltages, while conduction loss is becoming the dominant factor in higher DC link voltages. Figure 3.9 shows the total losses of the MMC for the annual loading shown in Figure 3.6 for varying DC link voltage (with 1 kV resolution).

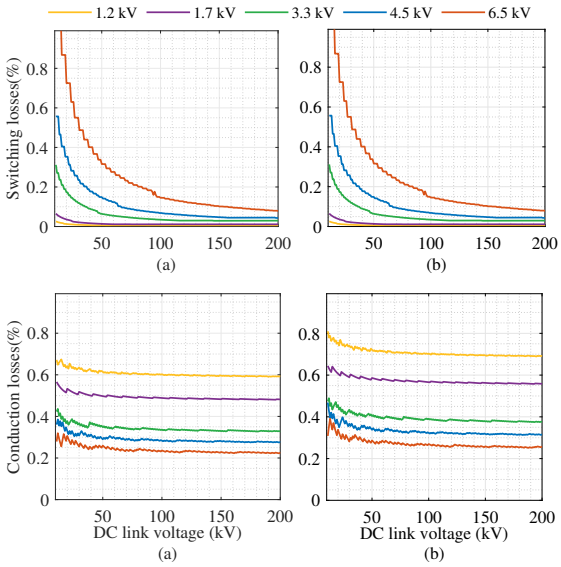

Figure 3.8: Losses of the MMC due to (a) switching losses in MP I (b) switching losses in MP II (c) conduction losses in MP I (d) conduction losses in MP II.

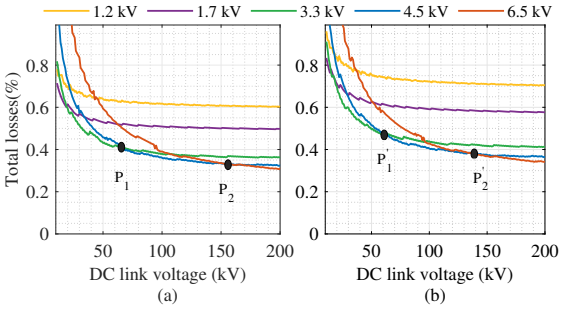

Figure 3.9: Total losses of the MMC for varying DC link voltage, (a) MP I and (b) MP II.

To better clarify the importance of annual loading, two points as P_1 and P_2 are considered from Figure 3.9. For MP I, the switch with a rated voltage of 4.5 kV is the most efficient for the DC link voltage range between $P_1 \approx 65$ kV to $P_2 \approx 157$ kV. However, this range is $P_1' \approx 62$ kV to $P_2' \approx 138$ kV when higher average loading corresponding to MP II is considered.

To generalize the scenarios mentioned in this sub-section for two different annual loading, an average annual loading point is considered, which can change from 1 % to 100 %. Figure 3.10 shows the heat map of the most efficient switch for varying DC link voltage and annual average loading. As it can be seen from Figure 3.10, for a DC link

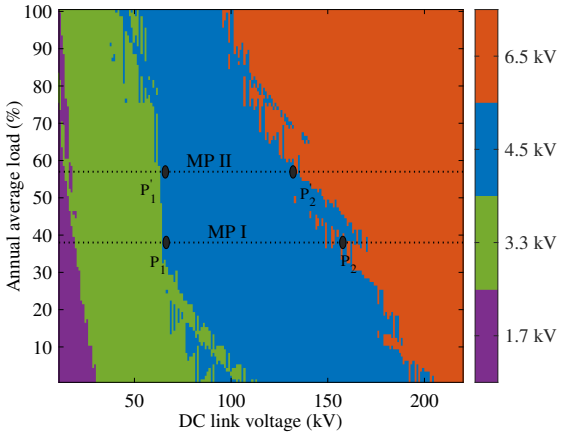

Figure 3.10: Optimal switch voltage rating choice map based on the efficiency of the MMC under various annual average loading with varying DC link voltage.

voltage higher than 200 kV, a switch with 6.5 kV rating voltage is the most efficient choice regardless of the average loading of the converter. For lower DC link voltages, there is a trend between an optimal switch dependent on the MMC's annual average loading. From Figure 3.10 can be seen that higher DC link voltage leads to a shift in preference towards higher rated voltage of switch for the same average yearly loading. Likewise, for the same DC link voltage, a higher annual load leads to a shift in preference toward a higher switch voltage rating. Please note that the energy savings obtained from constant average annual loading are slightly different when an hourly power demand of MMC is considered. This is shown in Figure 3.10 as points P_1, P_2, P_1', and P_2' obtained originally from hourly power demand in Figure 3.9. As it can be seen, the points are not exactly on the boundary between switches with 4.5 kV and 6.5 kV ratings, and it is slightly different.

3.4. SENSITIVITY ANALYSIS FOR GENERALIZED SWITCH VOLTAGE RATING SELECTION

As presented, many variables are needed to determine the most economical switch for every specific DC link voltage and annual average loading. Figure 3.11 summarizes the characteristic comparison of the MMC for three switches with rated voltage of 1.2, 3.3, and 6.5 kV. The trend shown in Figure 3.11 is valid for all DC link voltages and annual average loading. Nevertheless, combining all these characteristics defines the most economically viable choice for the rated voltage of the switch.

A financial index must be defined to compare different rated voltage of switches and find the economic viability range of each switch concerning DC link voltage and annual

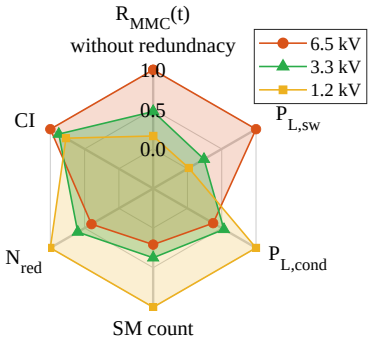

Figure 3.11: Overview of the trade-offs for 10 MW 17 kV DC link MMC affected by switch voltage rating.

average loading. This study considers payback as the economic index for determining the most economical switch choice. The payback helps make a financial decision based on how long it takes to get the profit for extra invested money. The CI and savings of the various switch choices are compared to calculate the payback as follows:

$$\text{Payback (PB)} = \frac{\Delta CI}{S_\text{i}} \tag{3.23}$$

$$S_\text{i} = \int \Delta E_i \times P_\text{t} \tag{3.24}$$

where ΔCI is the difference of CI between different switch ratings, S_i is the difference in cost saving due to efficiency, ΔE_i (kWh) is the energy saving difference, Pt is the price for electricity that in The Netherlands is equal to 0.190 €/kWh. In this study, the economic viability boundary is defined based on a considered payback time of 10 years. The steps given in the flowchart in Figure 3.12 can be followed to find the optimum rated voltage of the switch in the MMC with specified characteristics (DC link voltage and annual load demand). The methodology for finding the cost-efficient switch rating is shown in Figure 3.13. This algorithm evaluates if investing extra money in the MMC with the lowest CI to use other switch ratings could have a payback of 10 years or less.

Figure 3.14 presents the economic viability regions among various rated voltage of switches for $B_{10} = 10$ years with varying DC link voltage and annual average loading considering a 10-year payback. Similar to the obtained heat map of efficiency, the current and voltage rating of the switches are fixed. A comparison is performed among different rated voltage of switches. Figure 3.14 suggests that each rated voltage of the switches is more economically viable for a specific DC link voltage and loading. As presented in Figure 3.5 (a), the MMC with a rating voltage of 1.2 kV has the lowest CI, and Figure 3.14 shows if extra money invested in the MMC with higher switch voltage rating has a payback of 10 years or less. For instance, Figure 3.14 suggests that if the DC link voltage is 50 kV and the expected annual loading is 50 %, extra investment in the MMC that uses a switch with a rating voltage of 3.3 kV (instead of 1.2 kV and 1.7 kV) will have a payback of 10 years or less.

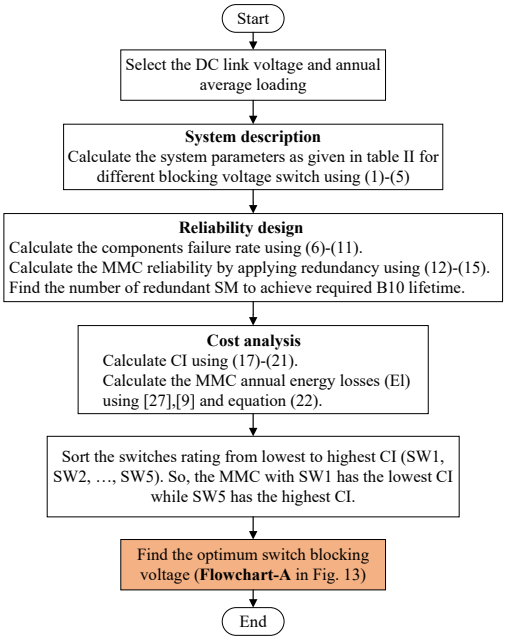

Figure 3.12: Flowchart of the proposed methodology for finding the optimum rated voltage of switch.

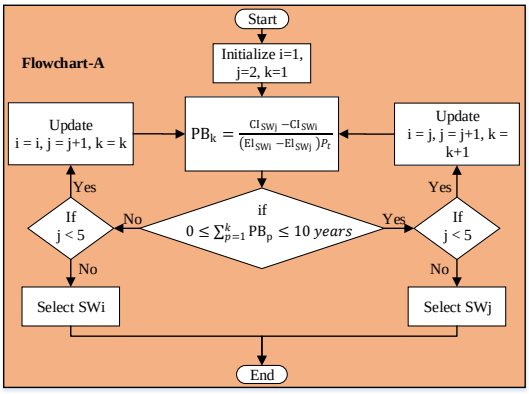

Figure 3.13: Algorithm for finding the optimum switch voltage rating among five options.

The two considered case studies are shown with dashed black lines in which fixed load is representative of annual average loading. From Figure 3.14 can be seen that in the case of MP II, the switch with a rated voltage of 1.7 kV is the most economical for the range of 10-22 kV DC link voltage. Regarding the case with MP I, 1.7 kV switch is economically viable for DC link voltages between 10 kV and 27 kV. Regarding extra investment in the switch with 3.3 kV rated voltage for MP II, the economically viable DC link voltage is estimated to be between 22 kV and 72 kV. For MP I, the estimated range is 27 kV to 83 kV.

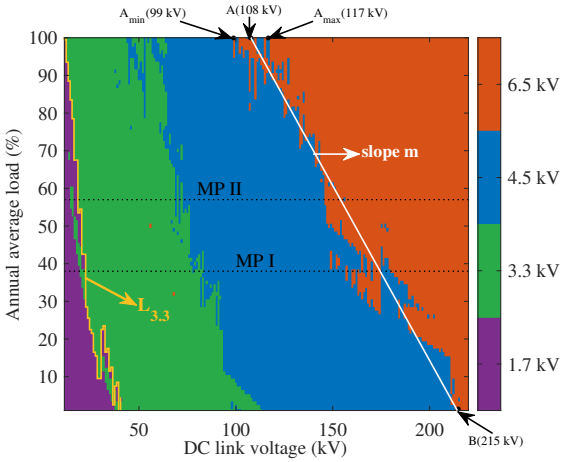

Figure 3.14: Economic viability region for different switch voltage rating with variation in MMC loading and DC link voltage considering a payback of 10 years and a required B_{10} = 10 years ($L_{3.3}$ is the boundary line between 1.7 kV and 3.3 kV switches).

The same economically viable DC link range can be estimated for the switches with rated voltage of 4.5 kV and 6.5 kV. Another example is 10 MW 17 kV DC link MMC in which the switch rating of 1.7 kV is the best choice, as shown in Figure 3.14. If the lifetime requirement is 10 years, using a switch with a 1.2 kV rating voltage results in lower initial cost (according to Figure 3.5). But, choosing a 1.7 kV switch leads to a 15% reduction in operational losses (according to Figure 3.9). Hence, in this case, the switch with the rated voltage of 1.7 kV is selected because the extra investment will have a payback of less than 10 years, and it is due to the higher efficiency.

3.4.1. Sensitivity Analysis for Different FR, B_{10} Lifetime Requirement, Components Cost and Energy Price

The sensitivity of the switch regions' payback to different B_{10} lifetime requirements, FR, component cost, and energy price is shown in Figure 3.15. The boundary line ($L_{3.3}$) between economic regions of 1.7 kV and 3.3 kV switches is considered since the same trend is valid for other boundary lines between other regions.

The required B_{10} lifetime can vary from 5 to 20 years. hence, the effect of higher or lower required B_{10} lifetime is shown in Figure 3.15 (a). As can be seen, there is no specific trend with an increase or decrease in the required B_{10} lifetime. As explained in Section 3.2 B, the methodology in MIL is used to estimate the FR of the IGBT and capacitor. However, the obtained values might not be precise as many environmental factors (π_x) can change the SM's actual FR. Moreover, there are other components within the structure of the SM, such as gate drives, control systems, and power supply, which might experience random failure. Therefore, for sensitivity analysis, the SM's FR's exact value is 20% higher and lower than the obtained values. It can be observed from Figure 3.15 (b) that the boundary line between regions of 1.7 kV and 3.3 kV switches has a limited dependence on the FR variation.

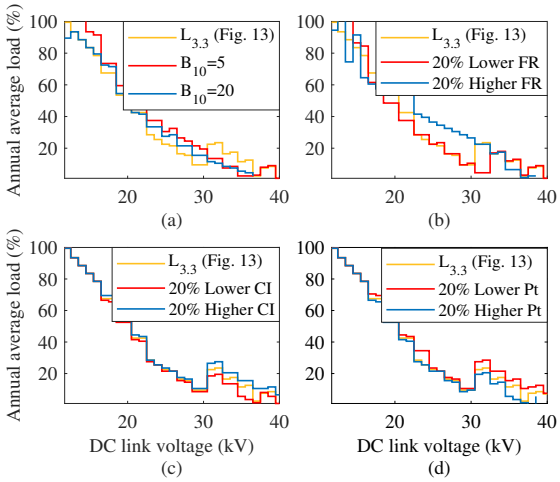

Figure 3.15: Shift in $L_{3.3}$ with change in (a) B_{10} lifetime; (b) FR; (c) capital investment (CI), and (d) electricity price (Pt).

Considering the component's cost, the dependence of the boundary line on CI is shown in Figure 3.15 (c). It can be realized that if components are more expensive, the boundary line ($L_{3.3}$) moves upwards quite trivially, and the economic viability region of the switch with 1.7 kV rated voltage (purple) increases. However, an increase in energy price has a reverse effect on the boundary line compared to the CI presented in Figure 3.15 (d), which is negligible.

3.4.2. SENSITIVITY ANALYSIS BY USING MIL AND FIDES

In this section, a more recent FIDES method [31] to calculate the FR of components (λ_{FIDES}) is compared with λ_{MIL} used thus far in the chapter. Unlike λ_{MIL}, λ_{FIDES} considers the technical control over manufacturing (Π_{pm}), field operation and maintenance (Π_{process}) and physical failure ($\lambda_{\text{physical}}$) that is given by (3.25) and (3.26).

$$\lambda_{\text{FIDES}} = \lambda_{\text{physical}} \times \Pi_{\text{pm}} \times \Pi_{\text{process}} \tag{3.25}$$

$$\lambda_{\text{physical}} = \sum_{i}^{\text{phases}} \left[\frac{t_{\text{annual}}}{8760} \right] \Pi_i \lambda_i \tag{3.26}$$

where t_{annual} denotes the duration of the i^{th} phase of the mission profile for one year. Π_i and λ_i are associated with environmental and operation stress-specific factors for each phase i. The complete methodology for FIDES is described in [31] and not repeated here for conciseness. Under assumptions corresponding to similar operating and environmental conditions, the estimated λ_{FIDES} compared with λ_{MIL} for the two mission profiles is shown in Table 3.4.

The sensitivity analysis is carried out to evaluate the impact of FIDES and MIL methods on the boundary line (i.e., $L_{3.3}$ in Figure 3.14). Table 3.4 shows that the FIDES method estimates the FR of components to be lower than MIL. Therefore, the shift in the bound-

Table 3.4: FR of the Capacitor and IGBT considering MIL and FIDES

Components	MP	FR (occ/year)	
		FIDES	MIL
IGBT	I	0.00052	0.0017
	II	0.00086	0.0022
Capacitor	I	0.00042	0.0009
	II	0.00068	0.0012

ary line ($L_{3.3}$) between regions of 1.7 kV and 3.3 kV switches can be seen in Figure 3.16. The sensitivity analysis represents that if the FIDES method is used for estimating the FR, the economic viability region of 1.7 kV switch expands for annual average loading of more than 30%.

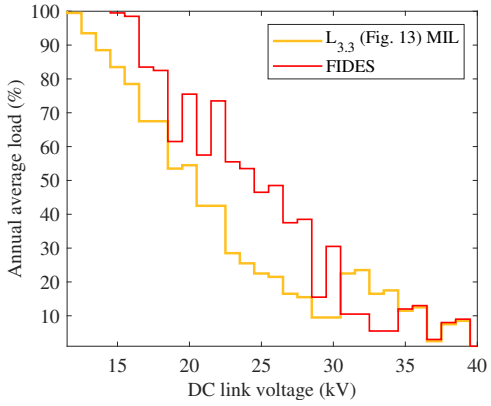

Figure 3.16: Shift in $L_{3.3}$ using FIDES and MIL to estimate the component's FR.

3.4.3. Impact of Converter Power Capacity

The selection of switch voltage rating for various DC link voltage and loading at a fixed rated capacity has been discussed. In this section, further evaluation is carried out to determine the most economically viable switch rating with variation in current rating and varying DC link voltage at 100% loading. As shown in Figure 3.17, the MMC-rated current is changed from 480 A to 1025 A, corresponding to the converter power rating from about 6.5 MVA to 275 MVA. From Figure 3.17, it can be observed that the switch rating selection is independent of rated current and only depends on loading and DC link voltage.

3.5. Generalized Application Specific Recommendations

MMC can be applied for different applications having different DC link voltage and current ratings[32]. The most economical switch voltage rating in these applications de-

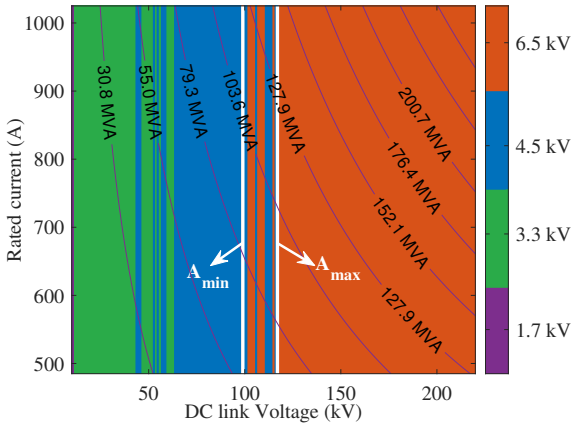

Figure 3.17: Economic viability region for different switch voltage rating with variation in MMC current rating and DC link voltage at 100% loading (i.e., 480 A, given in Figure 3.14) considering a payback of 10 years and a required $B_{10} = 10$ years.

pends on the selected DC link voltage and loading. In this context, to generalize the proposed method, equation (3.27) is derived from Figure 3.14.

$$\begin{cases} \text{if } \frac{\mathrm{L}}{100} + \mathrm{m}(V - V_{\mathrm{ref}}) \geq 0, & \text{Select the higher switch rating} \\ \text{else,} & \text{Select the lower switch rating} \end{cases} \tag{3.27}$$

where L is the annual average loading of the MMC in percentage, m and V_{ref} are specified in Table 3.5, and V is the considered DC link voltage. In Figure 3.14, a line with slope m connects two points (A, B) on boundaries between different switch ratings at 100 % and 1% loading. For instance, to find these two points between 4.5 kV and 6.5 kV switches at 100 % loading, the voltage rating is 108 kV. This voltage rating is calculated by taking the average of A_{min} and A_{max}, as shown in Figure 3.14. Thus, points A and B coordinate (108 kV, 100%) and (215 kV, 1%), respectively. Hence, the slope m can be calculated by having these two points.

For example, in [9], the DC link voltage is 54 kV, and the annual average loading is about 60 %. Since the DC link voltage is within the range of the second column of Table 3.5, the second column values are used. After putting these values in (3.27), it suggests that the most economical rated voltage of the switch is 3.3 kV. However, 4.5 kV switch is used in [9], which is overrated and can impact the cost and efficiency of the system. Table 3.6 summarizes some of the MMC applications found in the literature and shows the optimal rated voltage of the switch using the proposed method.

3.6. CONCLUSION

This chapter presents cost-oriented reliability and modularity-based trade-offs to select an optimal rated voltage of the switch for MMC. The steps involved in the proposed method are explained through flowcharts, and a heat map is provided for varying DC

Table 3.5: The Specifications of Equation (3.27)

Transition	$1.7 \leftrightarrow 3.3\,kV$	$3.3 \leftrightarrow 4.5\,kV$	$4.5 \leftrightarrow 6.5\,kV$
m	3.3×10^{-5}	2×10^{-5}	9×10^{-6}
V_{ref}	40 kV	110 kV	220 kV
Voltage range(kV)	$10 \leq V \leq 50$	$50 < V \leq 110$	$110 < V$

Table 3.6: Optimal switch voltage ratings for different applications

[Ref]	Application	V_{dc}	S_n	$P_{l,ave}$	V_{IGBT} (kV)	
		kV	MVA	%	Used	Optimal
[9]	MVDC Grid	±27	30	60	4.5	3.3
[6]	MVDC Grid	10	3	30	1.7	1.7
[7]	Wind	17	10	10-100 †	4.5	1.7/3.3
[30]	MVDC Grid	17	10	38 & 57	3.3	1.7
[15]	STATCOM	28	17	25-100 †	3.3	1.7/3.3
[17]	HVDC	±320	1000	-	4.5	6.5
[33]	Wind-HVDC	32	18	0-100 †	6.5	1.7/3.3
[34]	Wind-HVDC	160	320	-	3.3	4.5/6.5

† Variable power

link voltage and yearly loading of the MMC. It is presented that the system's modularity increases when a lower switch voltage rating is selected for the MMC SMs. For example, in a 10 MW MMC with a DC link voltage of 17 kV, a switch rating of 1.7 kV is optimal for both case studies. Higher modularity can be achieved with 1.2 kV rated voltage with a lower CI for a B_{10} lifetime of 10 years. But, when 1.7 kV switch is selected instead of 1.2 kV switch, the operational losses are approximately 15 % lower in both cases (MP I and MP II), leading to payback of less than 10 years. Higher DC link voltage leads to a shift in preference towards a higher switch rating for the same average loading. For example, the optimal choice of switch rated voltage changes from 1.7 kV to 3.3 kV in both case studies (MP I and MP II) if the given DC link voltage is increased from 17 kV to 50 kV. Transitions between preferred switch ratings with variation in DC voltages between 10-220 kV are shown for different average loading. The sensitivity analysis shows that the preference's boundary changes from 1.7 kV to 3.3 kV switch rating shifts downward slightly with lower CI and higher energy price. However, the preferred switch choices show limited sensitivity to variation in required B_{10} lifetime and assumed FR of individual components. Also, the preference's boundary from 1.7 kV to 3.3 kV shifts downward if FIDES methodology is used for estimating the components FR.

In conclusion, this study proposed selection regions for the optimum rated voltage of the switch in the MMC for varying DC link voltage and yearly load demand. Sensitivity analysis shows that for MMC with fixed-level active redundancy, the variation among switches' regions has limited dependence on the precise FR value and required B_{10} lifetime. Also, it was observed that changes in CI and energy prices have a negligible effect. However, using the methodology proposed in FIDES for calculating the FR can affect the

region as a specific trend was realized for annual loading higher than 30%. The effectiveness of the method proposed in this study is demonstrated by presenting a generalized version of it and applying it in published works.

REFERENCES

[1] J. Jia, G. Yang, and A. H. Nielsen, *A review on grid-connected converter control for short-circuit power provision under grid unbalanced faults,* IEEE Transactions on Power Delivery **33**, 649 (2018).

[2] R. Abe, H. Taoka, and D. McQuilkin, *Digital grid: Communicative electrical grids of the future,* IEEE Transactions on Smart Grid **2**, 399 (2011).

[3] S. Du, B. Wu, and N. Zargari, *Common-mode voltage minimization for grid-tied modular multilevel converter,* IEEE Transactions on Industrial Electronics **66**, 7480 (2019).

[4] S. Yang, A. T. Bryant, P. Mawby, D. Xiang, L. Ran, and P. J. Tavner, *An industry-based survey of reliability in power electronic converters,* IEEE Transactions on Industry Applications **47**, 1441 (2011).

[5] V. de Nazareth Ferreira, A. Fagner Cupertino, H. Augusto Pereira, A. Vagner Rocha, S. Isaac Seleme, and B. de Jesus Cardoso Filho, *Design and selection of high reliability converters for mission critical industrial applications: A rolling mill case study,* IEEE Transactions on Industry Applications **54**, 4938 (2018).

[6] P. Tu, S. Yang, and P. Wang, *Reliability- and cost-based redundancy design for modular multilevel converter,* IEEE Transactions on Industrial Electronics **66**, 2333 (2019).

[7] H. Li, X. Xie, A. McDonald, Z. Chai, T. Yang, Y. Wu, and W. Yang, *Cost and reliability optimization of modular multilevel converter with hybrid submodule for offshore dc wind turbine,* International Journal of Electrical Power & Energy Systems **120**, 105994 (2020).

[8] B. Wang, X. Wang, Z. Bie, P. D. Judge, X. Wang, and T. C. Green, *Reliability model of mmc considering periodic preventive maintenance,* IEEE Transactions on Power Delivery **32**, 1535 (2017).

[9] G. Abeynayake, G. Li, T. Joseph, J. Liang, and W. Ming, *Reliability and cost-oriented analysis, comparison and selection of multi-level mvdc converters,* IEEE Transactions on Power Delivery **36**, 3945 (2021).

[10] X. Xie, H. Li, A. McDonald, H. Tan, Y. Wu, T. Yang, and W. Yang, *Reliability modeling and analysis of hybrid mmcs under different redundancy schemes,* IEEE Transactions on Power Delivery **36**, 1390 (2021).

[11] J. Guo, X. Wang, J. Liang, H. Pang, and J. Gonçalves, *Reliability modeling and evaluation of mmcs under different redundancy schemes,* IEEE Transactions on Power Delivery **33**, 2087 (2018).

[12] J. Xu, H. Jing, and C. Zhao, *Reliability modeling of mmcs considering correlations of the requisite and redundant submodules,* IEEE Transactions on Power Delivery **33**, 1213 (2018).

[13] J. Xu, P. Zhao, and C. Zhao, *Reliability analysis and redundancy configuration of mmc with hybrid submodule topologies,* IEEE Transactions on Power Electronics **31**, 2720 (2016).

[14] J. Xu, L. Wang, D. Wu, H. Jing, and C. Zhao, *Reliability modeling and redundancy design of hybrid mmc considering decoupled sub-module correlation,* International Journal of Electrical Power & Energy Systems **105**, 690 (2019).

[15] J. V. M. Farias, A. F. Cupertino, V. d. N. Ferreira, H. A. Pereira, S. I. Seleme, and R. Teodorescu, *Reliability-oriented design of modular multilevel converters for medium-voltage statcom,* IEEE Transactions on Industrial Electronics **67**, 6206 (2020).

[16] J. E. Huber and J. W. Kolar, *Optimum number of cascaded cells for high-power medium-voltage ac–dc converters,* IEEE Journal of Emerging and Selected Topics in Power Electronics **5**, 213 (2017).

[17] J. Guo, J. Liang, X. Zhang, P. D. Judge, X. Wang, and T. C. Green, *Reliability analysis of mmcs considering submodule designs with individual or series-operated igbts,* IEEE Transactions on Power Delivery **32**, 666 (2017).

[18] R. Alvarez, M. Wahle, H. Gambach, and J. Dorn, *Optimum semiconductor voltage level for mmc submodules in hvdc applications,* in *2016 18th European Conference on Power Electronics and Applications (EPE'16 ECCE Europe)* (2016) pp. 1–9.

[19] K. Ilves, S. Norrga, L. Harnefors, and H.-P. Nee, *On energy storage requirements in modular multilevel converters,* IEEE Transactions on Power Electronics **29**, 77 (2014).

[20] J. V. M. Farias, A. F. Cupertino, H. A. Pereira, S. I. S. Junior, and R. Teodorescu, *On the redundancy strategies of modular multilevel converters,* IEEE Transactions on Power Delivery **33**, 851 (2018).

[21] A. Shekhar, L. B. Larumbe, T. B. Soeiro, Y. Wu, and P. Bauer, *Number of levels, arm inductance and modulation trade-offs for high power medium voltage grid-connected modular multilevel converters,* in *2019 10th International Conference on Power Electronics and ECCE Asia (ICPE 2019 - ECCE Asia)* (2019) pp. 1–8.

[22] J. He, Q. Yang, and Z. Wang, *On-line fault diagnosis and fault-tolerant operation of modular multilevel converters — a comprehensive review,* CES Transactions on Electrical Machines and Systems **4**, 360 (2020).

[23] *Reliability Prediction of Electronic Equipment: MIL-HDBK-217D.*, Military standardization handbook (Department of Defense, 1983).

[24] K. Hu, Z. Liu, Y. Yang, F. Iannuzzo, and F. Blaabjerg, *Ensuring a reliable operation of two-level igbt-based power converters: A review of monitoring and fault-tolerant approaches,* IEEE Access **8**, 89988 (2020).

[25] R. Billinton and R. N. Allan, *Reliability evaluation of engineering systems : concepts and techniques,* (1992).

[26] J. Falck, C. Felgemacher, A. Rojko, M. Liserre, and P. Zacharias, *Reliability of power electronic systems: An industry perspective,* IEEE Industrial Electronics Magazine **12**, 24 (2018).

[27] Y. Zhang, H. Wang, Z. Wang, Y. Yang, and F. Blaabjerg, *Impact of lifetime model selections on the reliability prediction of igbt modules in modular multilevel converters,* in *2017 IEEE Energy Conversion Congress and Exposition (ECCE)* (2017) pp. 4202–4207.

[28] H. Abu Bakar Siddique, A. R. Lakshminarasimhan, C. I. Odeh, and R. W. De Doncker, *Comparison of modular multilevel and neutral-point-clamped converters for medium-voltage grid-connected applications,* in *2016 IEEE International Conference on Renewable Energy Research and Applications (ICRERA)* (2016) pp. 297–304.

[29] A. Shekhar, T. B. Soeiro, Z. Qin, L. Ramírez-Elizondo, and P. Bauer, *Suitable submodule switch rating for medium voltage modular multilevel converter design,* in *2018 IEEE Energy Conversion Congress and Exposition (ECCE)* (2018) pp. 3980–3987.

[30] A. Shekhar, T. B. Soeiro, L. Ramírez-Elizondo, and P. Bauer, *Offline reconfigurability based substation converter sizing for hybrid ac–dc distribution links,* IEEE Transactions on Power Delivery **35**, 2342 (2020).

[31] *Fides guide 2009 edition a, "reliability methodology for electronic system", fides group, france, 2004.* .

[32] M. Priya, P. Pathipooranam, and M. Kola, *Modular multilevel converter topologies and applications - a review,* IET Power Electronics **12** (2019), 10.1049/iet-pel.2018.5301.

[33] H. Liu, K. Ma, Z. Qin, P. C. Loh, and F. Blaabjerg, *Lifetime estimation of mmc for offshore wind power hvdc application,* IEEE Journal of Emerging and Selected Topics in Power Electronics **4**, 504 (2016).

[34] G. Guo, H. Wang, Q. Song, J. Zhang, T. Wang, B. Ren, and Z. Wang, *Hb and fb mmc based onshore converter in series-connected offshore wind farm,* IEEE Transactions on Power Electronics **35**, 2646 (2020).

4

WP4: IPE MEASUREMENT OF GRID POWER QUALITY AND DATA SHARING

4.1. INTRODUCTION

Multi-domain simulation tools are essential for designing mechatronic (mechanics, electric, and electronics) systems and authenticating their operational characteristics [1]. Specifically for power electronics-based energy transition systems, complete life-cycle management can be accomplished using a Digital Twin (DT) that accurately reflects its operating states so as to map the physical body into a virtual body [2]. For developing DT, simulation applications are laying a crucial role. Furthermore, simulation tools are getting more powerful in the way that the behavior of a physical object can be determined due to physical force on it [3]. DT includes the use of simulation, workflows, and seamless simulation along with life cycle phases. From the simulation viewpoint, DT will be the next level in modeling, simulation, and optimization technology, as shown in Figure 4.1 [4].

In an attempt to clarify the distinction between a DT and a system model, [5] suggests that DT is the highest fidelity computation model that is as close to real-time as possible. Since there is no clearly defined boundary for the fidelity level of the model and clock time for this distinction, we can relax our definition to encompass all system models as fundamentally some form of DT representation of reality. However, Real-Time Digital Twin (RTDT) is a specific class of DTs required when a part of the physical system is integrated with it, as shown in Figure 4.2. The utility of such a test bed is that it effectively combines the flexibility of software simulation with the fidelity of a physical system in a real-time environment.

Such Power Hardware-in-the-Loop (PHIL) set-ups are a cost-effective and scalable means for de-risking experimental validation of the developed models [6]. Specifically,

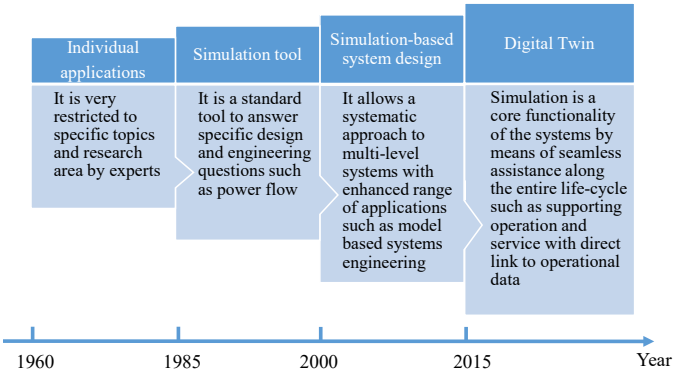

Figure 4.1: Different waves of simulation technology [4].

Figure 4.2: Concept diagram of RTDT interfaced physical system.

one or more of the following technical challenges are addressed by utilizing the RTDT-based PHIL test beds:

- Flexibility of RTDT offers a practical and scalable way of realizing very large systems such as electrical networks and high power/voltage multilevel converters. Furthermore, different test scenarios and configurations can be described in real-time simulation, which is difficult to achieve in a reasonable time frame in research labs.

- When fidelity of actual hardware is difficult or impossible to achieve through simulation. This aspect is particularly valid for reliability research because wear-out mechanisms are probabilistic and can never be modelled accurately.

- Real-time clocking is necessary to ensure response validity during fast transients, and random behaviors must be investigated. This is very important for the demonstration of innovative concepts at a higher Technological Readiness Level (TRL-3 or above).

The rest of the chapter is organized as follows: Some use cases for implementing RTDT-based PHIL testbed for research in reliable power electronic systems are discussed in Section 4.2. Finally, the conclusions are given in Section 4.3.

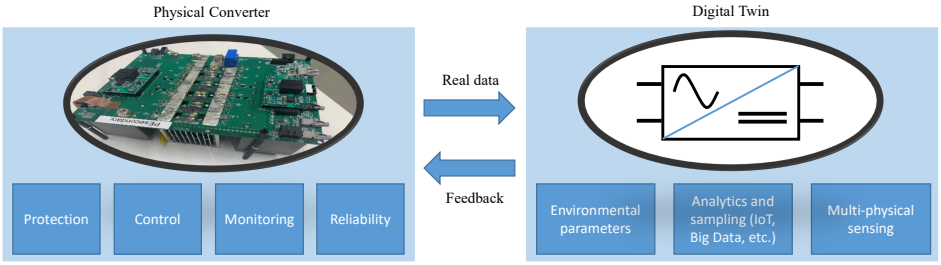

Figure 4.3: An overview of using DT for PECs.

4.2. USE CASES FOR POWER ELECTRONIC SYSTEMS

4.2.1. FAULT TOLERANT CONVERTERS

Most advanced simulators for Power Electronics Converters (PECs) are specified to address one specific problem or investigate a particular part of the system; hence, they result in different descriptions of simulators. Real-time emulation of device-level PEC models is critical by providing precision prediction of element stresses to lay out better control and protection methods. Developing a trustworthy, adequate, and cost-effective PEC requires multiple replications on costly and time-consuming hardware prototypes. Therefore, real-time hardware-in-the-loop (HIL) simulation systems such as DT can display a substantial role in getting the real system behavior and reducing the cost in the primary design stage. With PECs models, the system's primary circuit is created to evaluate the voltage and currents at various points. In PECs, the system is characterized by multiple requirements such as power transmission, harmonics, time-related load movement, electromagnetic compatibility, fault-tolerant operation, condition monitoring, etc. [7]. By applying DT, as shown in Figure 4.3, all previous problems can be addressed, and accurate models of PECs can be achieved [8].

PECs are susceptible to errors and may be exposed to mechanical vibrations and electromagnetic interference (EMI) since they contain a control portion, a power circuit, and different sensors, among other things. Due to these problems, fault detection and maintenance analysis in PECs has emerged as a crucial topic that can reduce deviations and transients. While offline simulations might aid in analyzing an uncommon scenario in a specific area, simulating numerous irregularities and defects throughout the entire PECs would be difficult. Therefore, using DT and real-time HIL in this field is crucial [7]. As previously stated, timely defect detection in PECs is essential for availability, reliability, and safety. It is crucial to gather, compile, and process precise data on the technical status of the equipment to reduce the failure risk in PECs. It can offer a forecast for any damage to the electric machinery. Following PECs infrastructure, condition monitoring is fault diagnosis and maintenance [7, 9].

4.2.2. ROBUST INTERFACE FOR GREEN TECHNOLOGIES

Power electronics for high-power electrolysis require careful design and consideration. The application's low voltage and extremely high current requirement impose constraints for component selection and selected topology of the converter interface [10, 11]. To

handle the significant operating current requirements, modular power electronics exhibit much potential. It can be time-consuming and costly to experimentally validate different system configurations and their robustness to different fault scenarios. Therefore, developing an RTDT-based PHIL testbed of such a system, as shown in Figure 4.4, is essential. A digital twin of the modular converter, along with an electrolyzer, can be modelled in a real-time simulator such as an OPAL-RT. One of the converter modules can be integrated as PHIL with this digital twin, as shown in Figure 4.4. The data such as stack voltage, current, and hydrogen production profile can also be shared in real-time if the electrolyzer is present as PHIL.

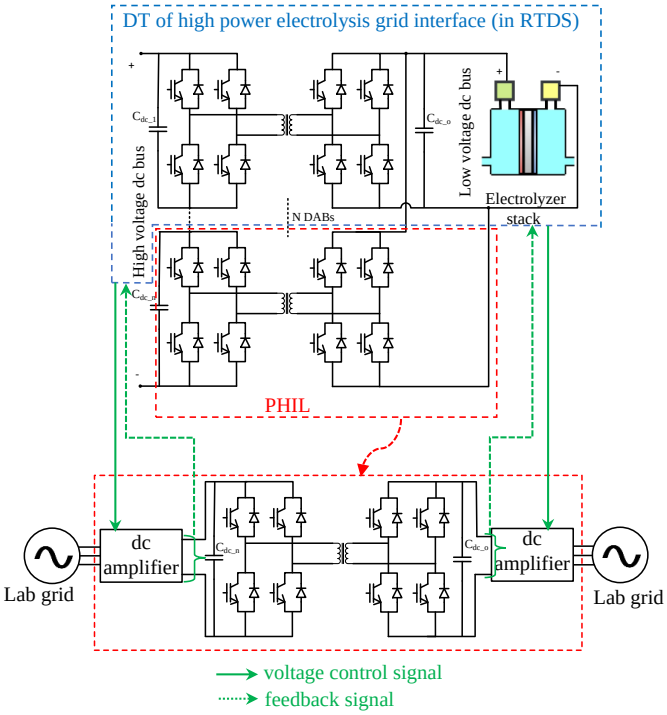

Figure 4.4: Power hardware-in-loop setup for robustness assessment of high power electrolysis grid interface.

4.2.3. PROTECTION OF MULTI-TERMINAL DC SYSTEMS

Stringent requirements of protection in DC systems restrict the process of fault isolation to a few milliseconds from fault inception [12]. Time-domain-based fault detection algorithms have merit (in comparison to traveling-wave-based methods) of robust performance against high-impedance faults using low computation [13]. As a trade-off, time-domain-based methods inherently depend on parameters (unit resistance, inductance, and capacitance) of overhead lines (OHL) and underground cables (UGC) for fault detection [13]. DC fault transients are low-frequency, meaning the maximum contribution in the total fault impedance is of the inductance of the line (in comparison to DC

steady state impedance, which is merely resistive). The contribution is further complemented by the external modification of current-limiting reactors (CLRs) used to limit the rate of rise of current upon a DC fault inception [12–14]. This means any variation in the true value of unit inductance may jeopardize the selectivity and dependability of time-domain-based fault detection algorithms [13].

Since regular monitoring of system parameters is inconvenient and challenging, a real-time DT of UGC and OHL would give accurate values of line or cable parameters. As shown in Figure 4.5, the inputs can be used to model the line or cable parameters in RTDS. The line parameters would be adaptively adjusted to their true values (r,l,c), which could be then used by the time-domain-based algorithms to detect faults in a multi-terminal DC system. This ensures the selectivity and dependability of the time-domain-based protection algorithms with the inherent merits of low computational burden and robust performance.

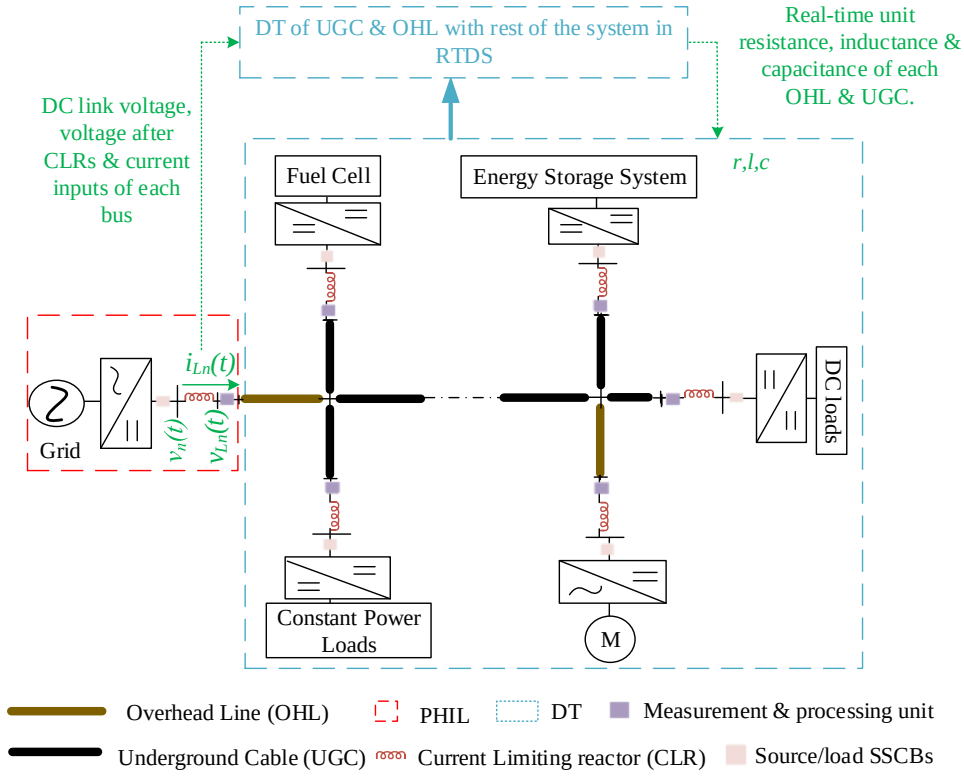

Figure 4.5: PHIL setup for selective and dependent protection of multi-terminal DC systems.

4.2.4. RECONFIGURABILITY IN HYBRID AC-DC LINKS

Reconfigurability in the hybrid AC-DC distribution links is being researched due to several benefits such as improved efficiency, increased reliability, enhanced flexibility, re-

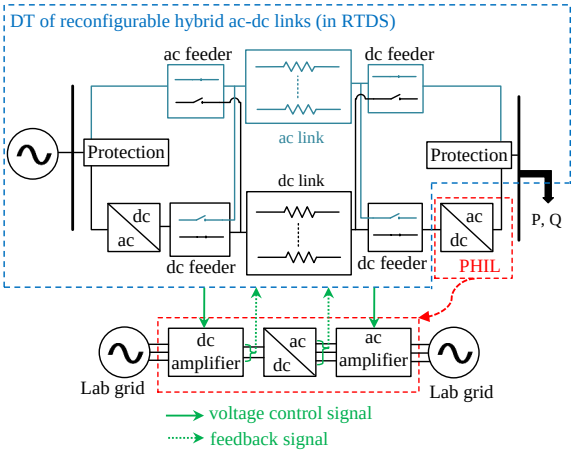

Figure 4.6: PHIL setup for reconfigurable hybrid ac-dc links.

duced costs, and improved power quality [15, 16]. A concept of offline reconfigurability of such a system is reported in [15]. However, implementing and testing such systems in real-time is challenging, complex, and costly. Therefore, the DT with PHIL of this system could be an alternative to test and validate the new configurations and algorithms for a real scenario. Figure 4.6 shows an example setup of DT with PHIL of reconfigurability in hybrid AC-DC links in case of faults and/or capacity enhancement during (n-1) contingencies. In Figure 4.6, a digital model of the link's hardware and software components, as well as a representation of the link's operating environment, is highlighted in the blue box, and the PHIL part (i.e., dc/ac converter) is in the red box. In PHIL, dc and ac amplifiers are used at the input and output of the dc/ac converter, respectively, and the power is fed back to the lab grid. The voltage control signals (marked in the green arrow) for dc and ac amplifiers are generated by DT, and the feedback signals are given back to the DT. This setup would be able to simulate and test the functioning of the link under a range of conditions, including variations in load levels and configurations of the link in case of link fault(s).

4.3. CONCLUSION

In this chapter, a real-time DT-based PHIL test bed for reliable PES has been explained, which is a cost-effective and time-efficient way to test the system under development. Some use cases applications such as fault-tolerant converters, power electronic interfaces for green technologies, protection of multiterminal dc systems, and reconfigurable hybrid ac-dc links have been discussed using this test bed. Thus, this work shows the potential use of a real-time DT-based PHIL test bed to research popular and new areas. In the future, a real-time DT-based PHIL of reconfigurable hybrid ac-dc links will be presented.

REFERENCES

[1] M. Ahmadi, H. J. Kaleybar, M. Brenna, F. Castelli-Dezza, and M. S. Carmeli, *Adapting digital twin technology in electric railway power systems,* in *2021 12th Power Electronics, Drive Systems, and Technologies Conference (PEDSTC)* (2021) pp. 1–6.

[2] H. Chen, Z. Zhang, P. Karamanakos, and J. Rodriguez, *Digital twin techniques for power electronics-based energy conversion systems: A survey of concepts, application scenarios, future challenges, and trends,* IEEE Industrial Electronics Magazine , 2 (2022).

[3] M. W. Grieves and J. Vickers, *Digital twin: Mitigating unpredictable, undesirable emergent behavior in complex systems,* (2017).

[4] S. Boschert and R. Rosen, *Digital twin—the simulation aspect,* (2016) pp. 59–74.

[5] M. Steurer, M. Stanovich, D. Soto, and V. Kane, *Incorporating hardware-in-the-loop simulation into a roadmap for the navy's digital twin paradigm,* Naval Engineers Journal **132**, 57 (2020).

[6] C. S. Edrington, M. Steurer, J. Langston, T. El-Mezyani, and K. Schoder, *Role of power hardware in the loop in modeling and simulation for experimentation in power and energy systems,* Proceedings of the IEEE **103**, 2401 (2015).

[7] Y. Peng, S. Zhao, and H. Wang, *A digital twin based estimation method for health indicators of dc–dc converters,* IEEE Transactions on Power Electronics **36**, 2105 (2021).

[8] G. Bhatti, H. Mohan, and R. Raja Singh, *Towards the future of smart electric vehicles: Digital twin technology,* Renewable and Sustainable Energy Reviews **141**, 110801 (2021).

[9] Y. Peng and H. Wang, *Application of digital twin concept in condition monitoring for dc-dc converter,* in *2019 IEEE Energy Conversion Congress and Exposition (ECCE)* (2019) pp. 2199–2204.

[10] R. S. Deshmukh, A. Shekhar, and P. Bauer, *Adaptive modularity for power electronics based electrolysis systems for green hydrogen,* in *2022 IEEE 20th International Power Electronics and Motion Control Conference (PEMC)* (2022) pp. 508–515.

[11] C. Pascalau, T. B. Soeiro, N. H. van der Blij, and P. Bauer, *Electrical energy conversion for low temperature electrolysis - challenges and future trends,* in *2021 IEEE 19th International Power Electronics and Motion Control Conference (PEMC)* (2021) pp. 349–356.

[12] V. Nougain, S. Mishra, and S. S. Jena, *Resilient protection of medium voltage dc microgrids against cyber intrusion,* IEEE Transactions on Power Delivery **37**, 960 (2022).

[13] V. Nougain and S. Mishra, *Current limiting reactors based time-domain fault location for high voltage dc systems with hybrid transmission corridors,* IEEE Transactions on Instrumentation and Measurement , 1 (2022).

[14] J. Xu, Y. Lü, C. Zhao, and J. Liang, *A model-based dc fault location scheme for multi-terminal mmc-hvdc systems using a simplified transmission line representation,* IEEE Transactions on Power Delivery **35**, 386 (2020).

[15] A. Shekhar, T. B. Soeiro, L. Ramírez-Elizondo, and P. Bauer, *Offline reconfigurability based substation converter sizing for hybrid ac–dc distribution links,* IEEE Transactions on Power Delivery **35**, 2342 (2020).

[16] A. Shekhar, L. Ramírez-Elizondo, T. B. Soeiro, and P. Bauer, *Boundaries of operation for refurbished parallel ac–dc reconfigurable links in distribution grids,* IEEE Transactions on Power Delivery **35**, 549 (2020).

5

WP-5: Case study and development of IPE components

5.1. Introduction

Targeting the goal of climate neutrality starts to strain the power transmission and distribution systems significantly [1, 2]. With the recent emergence of all-electric houses, heat pump systems, and e-mobility, the localised energy demand has grown significantly. Furthermore, energy consumption has shown an astringent pattern caused by electric vehicle charging [3]. On the other end, renewable generators like wind and photovoltaic possess the downsides of intermittency and unpredictability [2]. Power fluctuations on both the supply and demand side cause the curtailment of RES and put stresses on the power distribution infrastructure [4, 5]. All of these contribute toward the more frequent occurrence of congestions in domestic power grids [6, 7]. A commonly proposed solution for grid congestions is to incorporate DC links as a backbone to the existing AC power networks [8]. DC links provide enhanced power flow control, lower operating losses, and improved power transfer capacity over the ac alternative [9, 10]. Implementing DC links can enhance the overall grid stability and improve the utilisation of renewable energy sources by aggregating remote demand-supply imbalances [11, 12]. Also, existing ac links can be repurposed into DC links to enhance the transfer capacity of the given cable [13]. This improved utilisation of the existing grid infrastructure can fulfil the increasing load demand in densely populated areas.

Because of its characteristics, the modular multilevel converter (MMC) can be used to support an exciting medium voltage ac (MVAC) distribution network by incorporating two terminal medium-voltage dc (MVDC) distribution links [6]. The MMC is a highly efficient converter which can be used as an interface between an AC grid and a DC bus. It provides promising reliability and fault handling aspects while maintaining a highly scalable design [8]. The MMC-based MVDC distribution link, illustrated in Figure 5.1,

connects two possibly asynchronous ac networks (V_{g1},V_{g2}) via two back-to-back connected MMCs[14]. Normally, an MVDC link is operated at a fixed rated DC voltage, set through one of the MMCs. Though as proposed in [15], the distribution link can be operated at an enhanced DC voltage V_d that exceeds the rated value V_{dr} while maintaining the MMC performance under specific operating conditions. This is achieved while preserving the average stored energy in the MMC and the ac-side harmonic performance. Hence, the MMC can be operated at an enhanced DC voltage while encountering the same submodule (SM) stresses.

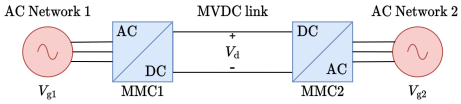

Figure 5.1: MVDC distribution link with back-to-back MMCs.

5

Operating the distribution link at an enhanced dc voltage while maintaining the rated current condition improves the power transfer capacity of the link, e.g. during grid congestions. Consequently, the same SM switch and capacitor voltage ratings achieve a link capacity enhancement. Alternatively, for a given operating power, the voltage enhancement can improve the efficiency of the link system by reducing the dc component of the circulating current.

In the present work, the voltage and capacity enhancement concepts are explained and verified using a simulation of a 10MW MVDC distribution link. In addition, it elaborates on the challenges encountered when implementing this enhancement in a practical DC distribution link. The rest of the chapter is organised as follows: Section 5.2 specifies the DC link system parameters and introduces the enhancement concept. Section 5.3, provides various simulation results, indicating the performance of the enhanced link system. Section 5.4 elaborates on the practical implementation concerns. Finally, conclusions are drawn in Section 5.5.

5.2. METHODOLOGY

5.2.1. SYSTEM DESCRIPTION

The simulated 10MW MMC-based MVDC link connects two 10kV ac distribution networks via back-to-back MMCs, forming a symmetrical monopolar configuration. The MMCs are configured along the double-star topology, as shown in Figure 5.2 [16]. The six MMC arms are each composed of 9 series connected half-bridge submodules and a 100μH arm inductance. The submodules are constructed using two 3.3kV IGBT switches and a 3.3mF capacitance. During the operation of the distribution link, the link current $i_{d,max}$ is thermally limited to 585A [9] and the rated DC voltage V_{dr} is set at 17.1kV to ensure compliance with the maximum modulation index as proposed in [17]. Regulating the MMC is a controller which is derived from [18, 19]. The system parameters used during the simulation are summarised in Table 5.1.

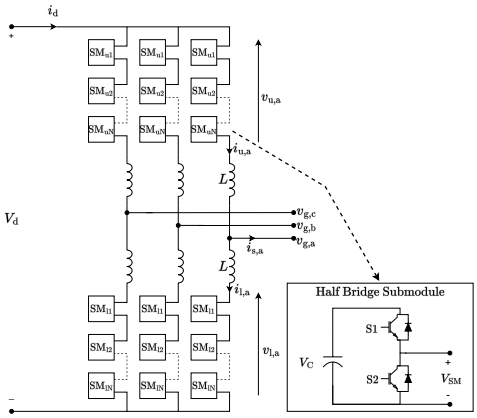

Figure 5.2: MMC schematic in double-star configuration.

5

Table 5.1: MVDC distribution link model parameters

System parameters:	**Symbol**	**Value**
Control frequency	f_c	10kHz
AC grid:		
Grid frequency	ω_1	314.2 rad/s
Grid voltage L-N (rms)	v_g	5.77kV
Grid inductance	L_g	287μH
Grid resistance	R_g	9mΩ
DC link:		
DC link resistance	R_l	0.1Ω
DC link inductance	L_l	100μH
Rated DC link voltage	V_{dr}	17.1kV
MMC:		
Rated apparent power	S_{max}	11MVA
Submodule capacitance	C	3.3mF
DC link capacitance	C_d	100μF
Number of arm submodules	N	9
Arm inductance	L	4mH
Arm resistance	R	0.1 Ω
Maximum output current	$i_{s,max}$	907A

5.2.2. ENHANCEMENT CONCEPT

As mentioned in [15], the DC link voltage enhancement considers two crucial quantities of the MMC: the arm voltage $v_{u,l}$ and the sum capacitor voltage $v^{\Sigma}_{cu,l}$. The arm voltage is defined as the potential across the arm submodule string and is characterised by (5.1). $v_{u,l}$ retains a common-mode phase-leg voltage of $0.5V_d$ and the sinusoidal output voltage of $\hat{v}_s \cos(\omega t)$.

$$v_{u,l} = v_c \mp v_s = \frac{1}{2} V_d \mp \hat{v}_s \cos(\omega t) \tag{5.1}$$

The sum capacitor voltage is defined as the sum total of the SM capacitor voltages in the respective arm, and is given by (5.2). $v^{\Sigma}_{cu,l}$ is controlled to have an average component V_d and has two ripple components caused by the total energy ripple ΔW_{Σ} and imbalance energy ripple ΔW_{Δ} as expressed in (5.3) and (5.4), respectively [19, 20]. Note that ΔW_{Σ} and ΔW_{Δ} depend on the operating power of the MMC.

$$v^{\Sigma}_{cu,l} \approx V_d + \frac{N}{2CV_d}(\Delta W_{\Sigma} + \Delta W_{\Delta}) \tag{5.2}$$

$$\Delta W_{\Sigma} = -\frac{\hat{V}_s \hat{I}_s}{4\omega_1} \sin(2\omega_1 t - \phi) \tag{5.3}$$

$$\Delta W_{\Delta} = \frac{V_d \hat{I}_s}{2\omega_1} \sin(\omega_1 t - \phi) - \frac{2\hat{V}_s i_c}{\omega_1} \sin(\omega_1 t) \tag{5.4}$$

To achieve the link enhancement, the DC voltage V_d is operated beyond the nominal value V_{dr}. Though, to preserve the converter performance, both the submodule stresses and the ac side harmonic character must remain equal to the rated condition. Following (5.1) and (5.2), the voltage enhancement corresponds to a biasing of the arm voltage $v_{u,l}$ while maintaining the average sum capacitor voltage $\overline{v^{\Sigma}_{cu,l}}$ at V_{dr}. This enhancement concept is illustrated in Figure 5.3. The figure contains the sum capacitor voltage and corresponding upper arm voltage for multiple operating DC link voltage values. In Figure 5.3 V_{dr} is considered as one p.u.

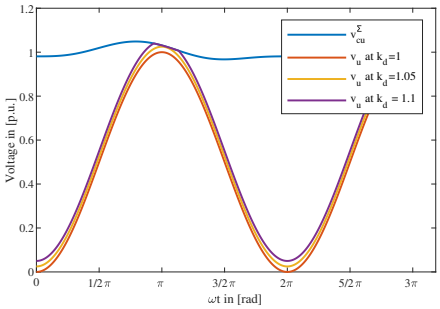

Figure 5.3: MMC steady state arm voltages.

It can be concluded from Figure 5.3 that the ripple in $v^{\Sigma}_{cu,l}$, caused by the arm's energy exchange, creates a positive spacing between the $v^{\Sigma}_{cu,l}$ and $v_{u,l}$ near $\omega t = \pi$. This ripple

margin can be used to bias $v_{u,l}$, while avoiding an intersection with $v^{\Sigma}_{cu,l}$. The DC component of $v_{u,l}$ can thus be increased by an enhancement factor k_d, causing an increase in the DC link voltage to $V_d = k_d V_{dr}$.

Though, observe from Figure 5.3 that the voltage enhancement is limited by the intersection of $v_{u,l}$ with $v^{\Sigma}_{cu,l}$. As this intersection of the arm voltage and sum capacitor voltage induces high-frequency arm voltage components, degrading the MMC's output harmonic performance. Eventually, this can lead to stability issues in the converter operation [21].

5.3. SIMULATION RESULTS

5.3.1. ARM VOLTAGES

To verify the workings of the DC link voltage enhancement, a simulation of the 10MW MMC-based MVDC distribution link is performed. The simulation is based on the arm-level averaged (ALA) model of an MMC, as introduced in [19, 22, 23]. The arm voltage and sum capacitor voltage of the phase a upper arm of MMC1 are simulated. Both MMC1 and MMC2 supply a reactive power Q of 3MVAr to the grid and together provide an active link power P of 10MW. Figure 5.4 shows the resulting $v_{u,l}$ and $v^{\Sigma}_{cu,l}$ for three values of the enhancement factor $k_d = \{1.0, 1.05, 1.1\}$. It can is concluded that transitioning from no DC voltage enhancement $k_d = 1.0$ to a small enhancement $k_d = 1.05$, the arm voltage is biased but maintains its sinusoidal shape. Meanwhile, the sum capacitor voltage is kept at the rated condition. This observation indicates a feasible 5% enhancement of the DC link voltage. Though, at an enhancement of $k_d = 1.1$ the arm voltage intersects the sum capacitor voltage and saturates. This flattening imposes a harmonic distortion in v_u, which causes distortion in the sinusoidal output voltage v_s. An excessive enhancement thus degrades the output harmonic performance of the MMC. This indicates that the proposed distribution link, operating at the given (P,Q), has a feasible voltage enhancement of $k_d = 1.05$ but fails to comply at $k_d = 1.1$.

5.3.2. ENHANCEMENT DEPENDENCIES

The voltage enhancement utilises the spacing between $v^{\Sigma}_{cu,l}$ and $v_{u,l}$ to facilitate the rise in V_d. The minimal value of this spacing is defined as the spacing voltage V_{space}, as given

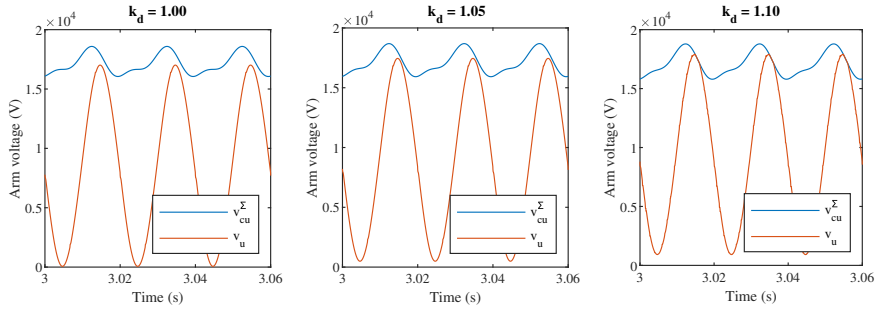

Figure 5.4: Simulated MMC arm voltages for different enhancement factors at 3MVAR and 10MW.

by (5.5). Observe in Figure 5.4 that a rise in k_d causes a biasing of v_u, which in turn results in a reduction of the spacing voltage. Furthermore, notice that if V_{space} becomes zero, harmonic components start to appear in the arm voltage, lowering the MMC ac side performance.

$$V_{space} = \min_{t\in[0,2\pi/\omega]} \left(v^{\Sigma}_{cu,l} - v_{u,l} \right) \tag{5.5}$$

To study the impact of the DC link voltage enhancement on V_{space}, a simulation is performed. The result is provided in Figure 5.5, which shows the spacing voltage as a function of the enhancement factor k_d for different values of Q and a constant value P at 10MW. From Figure 5.5 can be concluded that a negative correlation is encountered between the enhancement factor k_d and spacing voltage. In accordance with Figure 5.4, it is found that the spacing voltage is reduced in order to facilitate the enhancement of the DC side potential. Furthermore, V_{space} is shown to be positively correlated with the operating Q. This implies that V_{space} can be expanded by operating the converter at a larger reactive power. These two observations combined imply that for a fixed operating spacing voltage, e.g. 430V, an increase in Q enables a rise of the enhancement factor while maintaining the MMC performance. The exact solution of the enhancement factor as a function of reactive power Q is necessary to know but is not the focus of the current work.

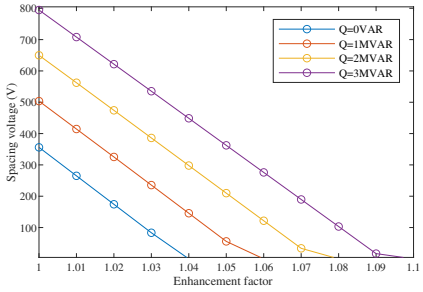

Figure 5.5: Spacing voltage at a constant 10MW active power.

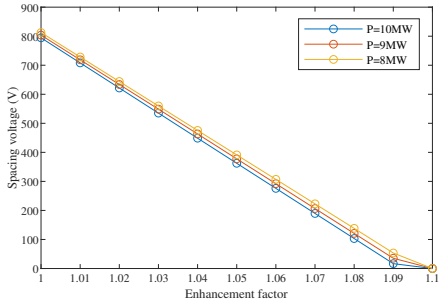

Figure 5.6: Spacing voltage at a constant 3MVAR reactive power.

A contrary observation is made from Figure 5.6, which shows the spacing voltage as a function of the enhancement factor k_d for different values of P and a constant reactive

power of 3MVAr. The graph indicates that the spacing voltage is nearly unaffected by the active power passing through the distribution link. This denotes that changes in V_{space} are dominated by changes in k_{d} and not P. For the practical operation of the distribution link, the MMCs are simulated with a modulation index of $m = 0.95$ in accordance with [17]. This caused a preliminary spacing voltage of 390V. This margin is crucial to handle the total- and imbalance energy ripple in $v^{\Sigma}_{\text{cu,l}}$ for different operating (P,Q). Besides, the spacing is utilised to prevent ac side harmonics injection during system transients. Therefore, a fixed positive V_{space} must be maintained throughout the enhancement to preserve the steady-state and transient ac-side harmonic performance. Using the concept of restricting the operating spacing voltage, the maximum DC voltage enhancement increases with the grid-injected reactive power and remains unaffected by the link's active power.

5.3.3. SM STRESSES AND HARMONIC PERFORMANCE

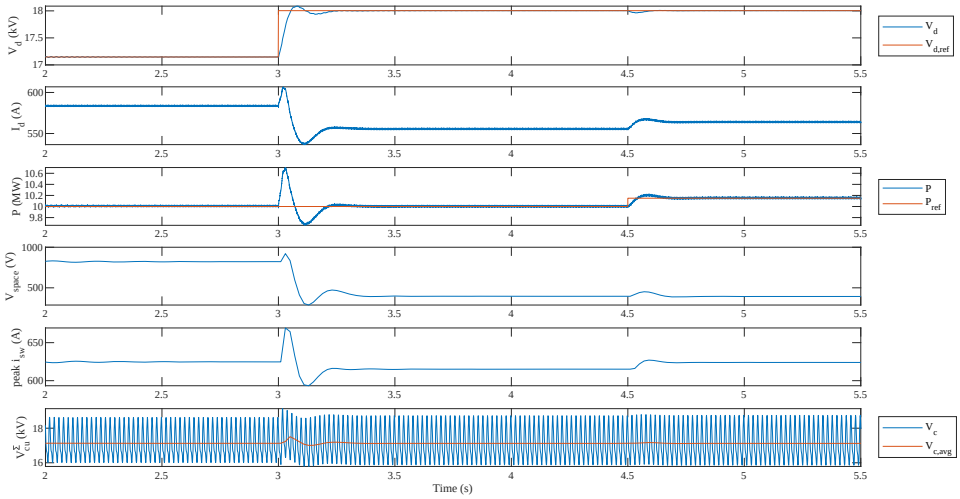

Figure 5.7: Performance of MMC-based DC link under voltage- and power enhancement.

Another system simulation is performed to verify the preservation of the submodule stresses and ac side harmonic performance under the DC voltage enhancement. Later this is extended to verify the MMC performance under a transfer capacity enhancement of the link. The simulation results are provided in Figure 5.7. This figure shows the DC link voltage V_{d}, DC link current I_{d}, active link power P, and the MMC1 spacing voltage, peak SM switch current, and sum capacitor voltage all as a function of time. The simulated variables show the response of the DC link system to a 5% voltage enhancement at $t = 3s$ (k_{d} from 1.00 to 1.05) and a 1.5% power enhancement at $t = 4.5s$ (k_{p} from 1.00 to 1.015). During the simulation, MMC1 and MMC2 supply a reactive power Q of 3MVAr to their corresponding ac network, and the link operates at a rated active power of 10MW.

It is observed in Figure 5.7 that for $t < 3s$, both the DC link voltage and sum capacitor voltage are in quasi steady state at the rated value of 17.1kV. Meanwhile, the DC link

current is constant at 584A to provide the active power transfer of 10MW. Notice that at the rated condition, the peak submodule switch current $\hat{i}_{sw}$ is 625A. After $t = 3s$, the DC link voltage reference is enhanced by 5% to 18.0kV. Figure 5.7 shows the dynamic transition of the V_d from its rated value to the enhanced reference. It can be observed that the spacing voltage V_{space} is reduced from 823V to 394V in order to facilitate this voltage enhancement. Because the active link power is maintained, the 5% voltage enhancement causes a 5% reduction in the link current to 556A. This 28A reduction contributes directly to a reduction of the DC circulating current component and lowers the peak submodule switch current from 625A to 615A. Following [12], this leads to an improved efficiency of MMC and corresponding link system. In Figure 5.7 can also be observed that the average sum capacitor voltage is controlled constant at the rated value of 17.1kV throughout the enhancement. Note that a downside of the voltage enhancement is the +1.2% increase in capacitor voltage ripple.

The simulation results of Figure 5.7 are summarised in Tables 5.2 and 5.3, which provide the MMC performance parameters regarding the currents and capacitor voltages, respectively. Table 5.2 also provides the total harmonic distortion (THD) of the MMC1's output current i_s before and after the voltage enhancement. It is noted that the THDi increases slightly from 0.419% before to 0.422% after the voltage enhancement. So overall the 5% voltage enhancement achieves a system efficiency gain while preserving the submodule switching stresses and maintaining the ac side harmonic performance of the MMC.

Table 5.2: MMC performance in enhanced operation: currents

k_d	k_p	AC side THD_i (%)		I_d (A)	Peak i_{sw} (A)	
1.00	1.00	0.4196	-	583.9	624.76	-
1.05	1.00	0.4226	+0.7%	555.7	615.12	-1.541%
1.05	1.015	0.4111	-2.0%	564.1	623.97	-0.126%
1.10	1.015	0.4606	+9.8%	538.2	616.69	-1.291%

Table 5.3: MMC performance in enhanced operation: capacitor voltage

k_d	k_p	Average $v^{\Sigma}_{cu,l}$ (kV)	Ripple $v^{\Sigma}_{cu,l}$ (kV)	Δ/μ of $v^{\Sigma}_{cu,l}$
1.00	1.00	17.12	2.61	15.2%
1.05	1.00	17.12	2.83	16.4%
1.05	1.015	17.12	2.88	16.8%
1.10	1.015	17.14	3.12	18.2%

At $t = 4.5s$, the power reference of the MMCs is enhanced from 10MW to 10.15MW. Figure 5.7 shows the dynamic transition of P from the rated to the enhanced value. It can be observed that the spacing voltage and DC link voltage remain nearly unaffected by active power change. Consequently, the link current i_d is enhanced to 564A to enable the active power enhancement. This increase in link current causes a rise in the DC circulating current component, which increases the peak submodule switch current to 624A. The average sum capacitor voltage is again controlled constant at the rated value of

17.1kV. Note that a downside of the power enhancement is the additional +0.4% increase in capacitor voltage ripple. The simulation results of Figure 5.7 are again summarised in Tables 5.2 and 5.3. From Table 5.2, it is noted that the THDi of MMC1 reduces slightly from 0.419% before to 0.411% after the power enhancement. So overall, the 1.5% active capacity enhancement is achieved while preserving the submodule switching stresses and maintaining the ac side harmonic performance of the MMC.

Additionally, Tables 5.2 and 5.3 summarise the performance parameters of a 10% voltage enhancement with a 1.5% power enhancement. This excessive enhancement causes the injection of output current harmonics, increasing the THDi by 9.8% compared to the rated operation. This observation is in line with the expectations and verifies the limit to the voltage enhancement. Combined, this set of simulations verifies that the DC link voltage enhancement can accommodate a transfer capacity enhancement in the MVDC distribution link while preserving the SM stresses and the ac side performance.

5.4. IMPLEMENTATION CHALLENGES

The previous two sections focus on the link enhancement concept, implying a set of assumptions that simplify the analysis. Though to integrate this concept in a practical MMC-based distribution link, a set of challenges is faced regarding the implementation and operation of the link system. This section elaborates on some of these challenges.

5.4.1. OPERATIONAL DISCREPANCIES

As discovered during the simulations, the set performance constraints limit the rise in the DC voltage. Though, when restricting the spacing voltage, the injection of reactive power extends the voltage enhancement limit. An important assumption made during the simulation is that both MMC1 and MMC2 of the DC link operate at the same reactive power. This operation is illustrated in case 1 of Figure 5.8. It was found that case 1 allows for a feasible 5% voltage enhancement.

However, an issue occurs if the MMCs operate at different reactive power references, as shown in case 2 of Figure 5.8. Following the result of Figure 5.5, it was found that an increase in Q led to an extension of the maximum k_{d}. This implies that the enhancement limit is bounded by the MMC operating at the lowest reactive power reference. So, in this scenario, MMC1 determines the limit to the voltage and power enhancement.

In case 3 of Figure 5.8, both MMCs operate at a reactive power of 3MVAr. Though MMC1 supplies reactive power to the AC network, whereas MMC2 consumes reactive power from the AC network. Following (5.2), (5.3), and (5.4), it is discovered that an MMC consuming reactive power reduces the spacing voltage below the rated condition. This effectively fixes k_{d} at the lower limit of 1 when the MMC operates at a lagging pf, to ensure compliance with the performance constraints. Combining the three cases leads to the definition of (5.6), in which f_{kd} is an empirical function converting Q into the operating enhancement factor.

$$k_{\mathrm{d}} = \max\{1, f_{\mathrm{kd}}(\min\{Q_1, Q_2\})\} \tag{5.6}$$

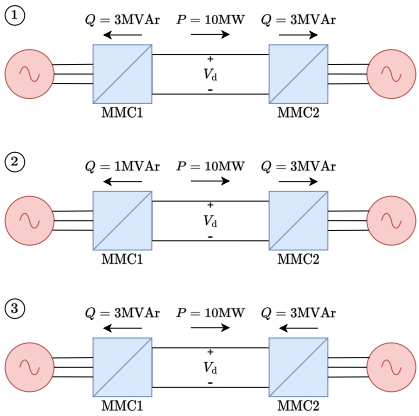

Figure 5.8: Operating cases of the DC link system.

5

5.4.2. DESIGN DISCREPANCIES

Another challenge with integrating the enhancement concept in the distribution link system relates to the MMC configuration. Till now, the DC link system was assumed to be in a symmetrical monopolar configuration, where MMC1 and MMC2 have the same structure. Though in practical implementations, the two MMCs might deviate in the number of submodules N and the submodule capacitance C. Notice from (5.2) that the sum capacitor voltage ripple is directly proportional to N. Similarly, the ripple in $v^{\Sigma}_{c,u}$ is inversely propositional to C. As this ripple directly affects the spacing voltage, it can be concluded that the MMC with the lowest N to C ratio determines the limit of k_d when both MMCs operate at the same Q.

5.4.3. DYNAMIC OPERATION

Another implementation challenge concerns the dynamic character of the enhanced link system. With practical grid-tied converters, reference changes can occur for both P and Q. Note that the enhancement limit depends on the reactive operating power of the MMC. Therefore any reference change in Q should be done cautiously considering the operated enhancement. For a dynamic implementation of the DC link enhancement, a controller must regulate k_d, k_p and Q based on an input reference Q^*. As k_p is admissible due to voltage enhancement k_d and k_d is admissible due to the reactive operating power Q, a dependency is imposed. This causes a strict dynamic order for changing k_d, k_p and Q upon a reference change Q^*. When the MMC operates in an enhanced voltage state, an increase of Q can directly be performed. Once Q has reached its steady state, k_d can be increased. Then upon the settling of V_d, k_p can be enhanced. This process is reflected in (5.7).

$$\text{Increase in } Q^* : \ [Q \uparrow] \Rightarrow [k_d \uparrow] \Rightarrow [k_p \uparrow] \tag{5.7}$$

Note that any other order of increasing the three parameters leads to either the injection of harmonic output current components or a significant increase in the peak SM

switch current. Alternatively, when the MMC operates in an enhanced voltage state, a decrease of Q can only be done after a significant lowering of V_{d}. Otherwise, harmonic output current components are injected into the AC grid. Though, to allow for the decrease in V_{d}, k_{p} must have been lowered accordingly. Otherwise, the peak SM switch current can exceed the limiting value. This process is reflected in (5.8).

$$\text{Decrease in } Q^{*}: \ [k_{\mathrm{p}} \downarrow] \Rightarrow [k_{\mathrm{d}} \downarrow] \Rightarrow [Q \downarrow] \tag{5.8}$$

The dynamic control procedure alters the operating k_{d}, k_{p} and Q in a stepwise manner. One method to achieve the result is with tuneable time parameters τ_{kd}, τ_{kp} and τ_{Q}. These reflect the maximum settle time of the corresponding variable to an input reference change. The controller concept is a stable and reliable design philosophy, favouring no constrain violation over dynamic performance.

5.5. CONCLUSIONS AND FUTURE WORK

When operating an MMC-based DC link, the energy ripple components in the capacitor voltage induce a spacing between the MMC arm voltage and the sum capacitor voltage. This margin can be used to enhance the DC link voltage and increase the transfer capacity of the distribution link system. Using a simulation model of a 10MW MVDC link, it is concluded that a 5% DC voltage enhancement can be realised while keeping the SM stresses at the rated condition and preserving the ac-side harmonic performance. This allows the distribution link voltage enhancement to be implemented with the same submodule switch and capacitor voltage ratings. The simulation was then successfully extended to verify the capacity enhancement. It is concluded that a 1.5% transfer capacity enhancement can be achieved in the 10MW DC link when restricting the switching currents to a below-rated condition. Furthermore, it was found from the simulations that the enhancement limit of the link increases with the MMC's grid-injected reactive power and remains unaffected by the link's active power. This observation defined the basis of the implementation challenges and the proposed control strategy for dynamic enhanced operation.

As part of future work, an analytical analysis should be performed to unveil the dependency between the enhancement factor limit and gird-inject reactive power. This notion can then be used to maximise the operating voltage enhancement while preserving MMC performance. In addition, it would form the basis of the high-level controller, providing a dynamic enhanced operation of the link system. Another aspect of future work relates to the application of voltage enhancement. The enhancement should be applied to bipolar DC links and multi-terminal MMC-based grids to increase the concept's impact in practical applications.

REFERENCES

[1] H. Schermeyer, M. Studer, M. Ruppert, and W. Fichtner, "Understanding Distribution Grid Congestion Caused by Electricity Generation from Renewables" in International Conference on Smart Energy Research, Essen, DE, 2017, pp. 78-89.

[2] Z. Dalala, M. Al-Omari, M. Al-Addous, M. Bdour, Y. Al-Khasawneh, and M. Alka-

srawi, “Increased renewable energy penetration in national electrical grids constraints and solutions” Energy, vol. 246, Feb 2022.

[3] N. Paterakis, M. Gibescu “A methodology to generate power profiles of electric vehicle parking lots under different operational strategies” in Applied Energy, vol. 173, pp. 111-123, Apr 2016.

[4] Y. Gu and L. Xie, "Fast Sensitivity Analysis Approach to Assessing Congestion Induced Wind Curtailment," in IEEE Transactions on Power Systems, vol. 29, no. 1, pp. 101-110, Jan. 2014, doi: 10.1109/TPWRS.2013.2282286.

[5] T. Xu, W. Gao, F. Qian and Y. Li, " The implementation limitation of variable renewable energies and its impacts on the public power grid," in Energy, vol. 239, Part A, Jan. 2022.

[6] S. Khuntia, B. Tuinema, J. Rueda, José, M. van der Meijden, “ Time-horizons in the planning and operation of transmission networks: an overview” in IET Generation, Transmission & Distribution, vol. 10, no. 4, pp. 841–848, Oct 2016

[7] R. A. Verzijlbergh, L. J. De Vries and Z. Lukszo, "Renewable Energy Sources and Responsive Demand. Do We Need Congestion Management in the Distribution Grid?," in IEEE Transactions on Power Systems, vol. 29, no. 5, pp. 2119-2128, Sept. 2014, doi: 10.1109/TPWRS. 2014.2300941.

[8] N. Ahmed et al., "HVDC SuperGrids with modular multilevel converters — The power transmission backbone of the future," International Multi-Conference on Systems, Signals & Devices, Chemnitz, Germany, 2012, pp. 1-7, doi: 10.1109/SSD.2012.6198119.

[9] A. Shekhar, E. Kontos, L. Ramírez-Elizondo, A. Rodrigo-Mor, and P. Bauer, “Grid capacity and efficiency enhancement by operating medium voltage AC cables as DC links with modular multilevel converters” in Electrical Power and Energy Systems, vol. 93, pp. 479-493, Jun 2017.

[10] Whitepaper, “MVDC PLUS Medium voltage direct current - Managing the future grid,” in Siemens AG, 2017.

[11] A. Shekhar, E. Kontos, L. Ramírez-Elizondo and P. Bauer, "AC distribution grid reconfiguration using flexible DC link architecture for increasing power delivery capacity during (n-1) contingency," 2017 IEEE Southern Power Electronics Conference (SPEC), Puerto Varas, Chile, 2017, pp. 1-6, doi: 10.1109/SPEC.2017.8333559.

[12] A. Shekhar, T. B. Soeiro, L. Ramírez-Elizondo and P. Bauer, "Weakly Meshing the Radial Distribution Networks with Power Electronic Based Flexible DC Interlinks," 2019 IEEE Third International Conference on DC Microgrids (ICDCM), Matsue, Japan, 2019, pp. 1-8, doi: 10.1109/ICDCM45535.2019.9232727.

[13] A. Shekhar, L. Ramírez-Elizondo, T. B. Soeiro and P. Bauer, "Boundaries of Operation for Refurbished Parallel AC–DC Reconfigurable Links in Distribution Grids,"

in IEEE Transactions on Power Delivery, vol. 35, no. 2, pp. 549-559, April 2020, doi: 10.1109/TPWRD.2019.2915198.

[14] M. Saeedifard and R. Iravani, "Dynamic Performance of a Modular Multilevel Back-to-Back HVDC System," in IEEE Transactions on Power Delivery, vol. 25, no. 4, pp. 2903-2912, Oct. 2010.

[15] A. Shekhar, L. Ramírez-Elizondo, Z. Qin, and P. Bauer, “Modular Multilevel Converter Performance with Dynamic MVDC Distribution Link Voltage Rating,” in 18TH International Conference on Power Electronics and Motion Control, Budapest, HU, 2018, pp. 1000–1005.

[16] S. Debnath, J. Qin, B. Bahrani, M. Saeedifard and P. Barbosa, "Operation, Control, and Applications of the Modular Multilevel Converter: A Review," in IEEE Transactions on Power Electronics, vol. 30, no. 1, pp. 37-53, Jan. 2015.

[17] Y. Li, X. Shi, B. Liu, F. Wang, and W. Lei, “Maximum modulation index for modular multilevel converter with circulating current control” in IEEE Energy Conversion Congress and Exposition, Pittsburgh, US, 2014, pp. 491–498.

[18] L. Angquist, A. Antonopoulos, D. Siemaszko, K. Ilves, M. Vasiladiotis, and H.-P. Nee, “Open-loop control of modular multilevel converters using estimation of stored energy,” IEEE Transactions on Industry Applications,vol. 47, no. 6, pp. 2516–2524, Nov./Dec. 2011.

[19] K. Sharifabadi, L. Harnefors, H. Nee, S. Norrga, and R. Teodorescu, Design, Control, and Application of Modular Multilevel Converters for HVDC Transmission Systems, First edition, Chichester: John Wiley & Sons, 2016.

[20] Q. Song, W. Liu, X. Li, H. Rao, S. Xu and L. Li, "A Steady-State Analysis Method for a Modular Multilevel Converter," in IEEE Transactions on Power Electronics, vol. 28, no. 8, pp. 3702-3713, Aug. 2013.

[21] Z. Liu, K. -J. Li, Z. Guo, J. Wang and J. Qian, "A Comprehensive Study on the Modulation Ratio for Modular Multilevel Converters," in IEEE Transactions on Industry Applications, vol. 58, no. 3, pp. 3205-3216, May-June 2022.

[22] J. Xu, A. M. Gole and C. Zhao, "The Use of Averaged-Value Model of Modular Multilevel Converter in DC Grid," in IEEE Transactions on Power Delivery, vol. 30, pp. 519-528, April 2015.

[23] J. Peralta, H. Saad, S. Dennetiere, J. Mahseredjian and S. Nguefeu, "Detailed and averaged models for a 401-level MMC-HVDC system," in IEEE Power & Energy Society General Meeting, 2013, pp. 1501-1508.

6

CONCLUSION

Chapter 1 has introduced the background for this work. Based on this, various objectives have been set, such as mapping electrical requirements of loads, developing design rules for power electronic systems to meet electrical requirements, developing methods for monitoring power quality in a specific part of the grid, etc. From these objectives, the expected results for this project have been given. Finally, the outline of the report is provided.

To understand the urban network performance on power quality, it is important to know every detail of electrical sources and loads. Therefore, Chapter 2 has presented the state-of-the-art electrolyzer and modeling of the alkaline electrolyzer. It also includes a review of converter topologies for their integration into the medium voltage DC grid. Moreover, the concept of adaptive modularity for power electronics converters employed in green hydrogen production has been introduced. This chapter further discussed the three potential configurations based on the DAB converter and explored the benefits of applying adaptive modularity to these configurations.

In Chapter 3, generalized design rules based on cost-oriented reliability and modularity-based trade-offs have been proposed to select an optimal rated voltage of the switch for MMC. Moreover, this chapter also proposed selection regions for the optimum rated voltage of the switch in the MMC for varying DC link voltage and annual load demand. It is presented with an example in a 10 MW MMC that the system's modularity increases when a lower switch voltage rating is selected for the MMC SMs. Moreover, it is found that DC link higher voltage leads to a shift in preference towards a higher switch rating for the same average loading. For example, the optimal choice of switch-rated voltage changes from 1.7 kV to 3.3 kV in both case studies (MP I and MP II) if the given DC link voltage is increased from 17 kV to 50 kV. As well, sensitivity analysis shows that for MMC with fixed-level active redundancy, the variation among switches' regions has limited dependence on the precise FR value and required B_{10} lifetime. Also, it was observed that changes in CI and energy prices have a negligible effect. Finally, the proposed design rules have been applied to existing works of literature to verify their effectiveness.

In Chapter 4, a real-time DT-based PHIL test bed for reliable PES has been presented.

Some use cases for the diverse power electronic applications have been discussed using this test bed. These applications include fault-tolerant converters, power electronic interfaces for green technologies, protection of multiterminal dc systems, and reconfigurable hybrid ac-dc links.

In Chapter 5, a control strategy has been proposed for the voltage and capacity enhancement and verified using a 10MW MVDC distribution link simulation. From the simulation model of a 10MW MVDC link, it is observed that a 5% DC voltage enhancement can be realized while keeping the SM stress at the rated condition and preserving the ac side harmonic performance. Moreover, the simulation is extended to verify the capacity enhancement. It is found that a 1.5% transfer capacity enhancement can be achieved in the 10MW DC link when restricting the switching currents to a below-rated condition. Furthermore, it was also found that the enhancement limit of the link increases with the MMC's grid-injected reactive power and remains unaffected by the link's active power. This observation defined the basis of the implementation challenges and the proposed control strategy for dynamic enhanced operation.

List of Publications

1. C. Pascalau, T. B. Soeiro, N. H. van der Blij and P. Bauer, "Electrical Energy Conversion for Low Temperature Electrolysis - Challenges and Future Trends," 2021 IEEE 19th International Power Electronics and Motion Control Conference (PEMC), Gliwice, Poland, 2021, pp. 349-356.

2. R. S. Deshmukh, A. Shekhar and P. Bauer, "Adaptive Modularity for Power Electronics Based Electrolysis Systems for Green Hydrogen," 2022 IEEE 20th International Power Electronics and Motion Control Conference (PEMC), Brasov, Romania, 2022, pp. 508-515.

3. V.A. Martinez Lopez, U. Žindžiūtė, H. Ziar, M. Zeman and O. Isabella, "Study on the Effect of Irradiance Variability on the Efficiency of the Perturb-and-Observe Maximum Power Point Tracking Algorithm", Energies, 15(20), 7562, 2022.

4. V.A. Martinez Lopez, H. Ziar, J.W. Haverkort, M. Zeman and O. Isabella, "Dynamic operation of water electrolyzers: A review for applications in photovoltaic systems integration", Renewable and Sustainable Energy Reviews, 2023 (accepted for publication).

5. V.A. Martinez Lopez, H. Ziar, M. Zeman and O. Isabella, "Maximization of PV energy use and performance analysis of a stand-alone PV-hydrogen system", (submitted, under review).

6. V.A. Martinez Lopez, G. van Urk, P.J.F. Doodkorte, M. Zeman, O. Isabella and H. Ziar, "Using sky-classification to improve the short-term prediction of irradiance with sky images and convolutional neural networks", (submitted, under review).

7. M. Ahmadi, A. Shekhar and P. Bauer, "Switch Voltage Rating Selection Considering Cost-Oriented Redundancy and Modularity-based Trade-offs in Modular Multilevel Converter," in IEEE Transactions on Power Delivery, 2023, doi: 10.1109/TPWRD.2023.3263270.

8. M. Ahmadi, A. Shekhar and P. Bauer, "Comparison of Military Handbook and the FIDES Methodology for Failure Rate Estimation of Modular Multilevel Converters", 2023 17th International Conference on Compatibility, Power Electronics and Power Engineering, Estonia, 2023 (accepted for publication).

9. A. Shekhar, G. Rituraj, R. v. d. Sande, M. Ahmadi, R. S. Deshmukh, V. Nougain, A. Lekić, P. Palensky and P. Bauer "Development of Reliable Power Electronic Systems using Real Time Digital Twin Based Power Hardware-in-the-Loop Testbed", 2023 IEEE PowerTech conference, Belgrade, 2023 (accepted for publication).

10. R. v. d. Sande, R. S. Deshmukh, A. Shekhar and P. Bauer "DC Link Capacity Enhancement for MMC-based Distribution Link Using Dynamic Voltage Operation", 2023 IEEE 11th International Conference on Power Electronics-ECCE Asia, Korea, 2023 (accepted for publication).